Influences of Space Weather Forecasting Uncertainty on Satellite Conjunction Assessment

William Parker[1], Mervyn P. Freeman[2], Gareth Chisham[2], Andrew John Kavanagh[2], Peng Mun Siew[1], Victor Rodriguez-Fernandez[3], and Richard Linares[1]

[1]Massachusetts Institute of Technology
[2]British Antarctic Survey
[3]Universidad Politecnica de Madrid

December 10, 2023

Abstract

A significant increase in the number of anthropogenic objects in Earth orbit has necessitated the development of satellite conjunction assessment and collision avoidance capabilities for new spacecraft. Often, the greatest source of uncertainty in predicting a satellite's trajectory in low Earth orbit originates from atmospheric neutral mass density variability caused by enhanced geomagnetic activity and solar EUV absorption. This work investigates the impacts of solar and geomagnetic index forecasting uncertainty on satellite drag and satellite maneuver decision-making. During an averaged point in the solar cycle, accurate index forecasts with reduced uncertainty are shown to provide significantly improved advance notice for dangerous conjunction events above 500 km. Below 500 km, forecast improvements are less impactful. This boundary of utility from forecast improvements shifts upward and downward during solar maximum and solar minimum, respectively. Improved index forecasts are shown to have little impact on making maneuver decisions 12-24 hours from a potential conjunction event, but are demonstrated to be very useful when trying to make maneuver decisions with more lead time. These improved forecasts of the space weather indices help in making actionable, durable conjunction predictions sooner than is currently possible.

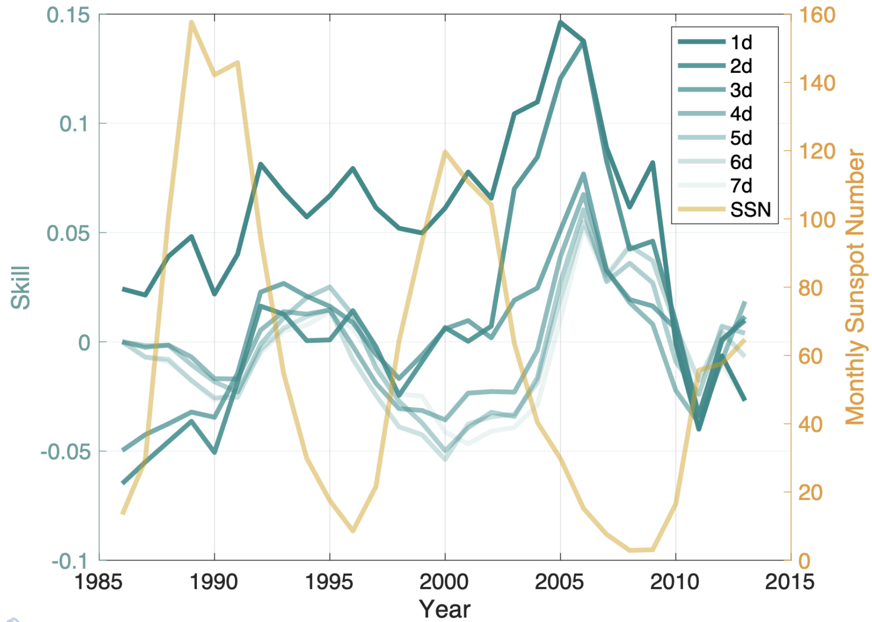

Skill
Monthly Sunspot Number
Year
1d
2d
3d
4d
5d
6d
7d
SSN

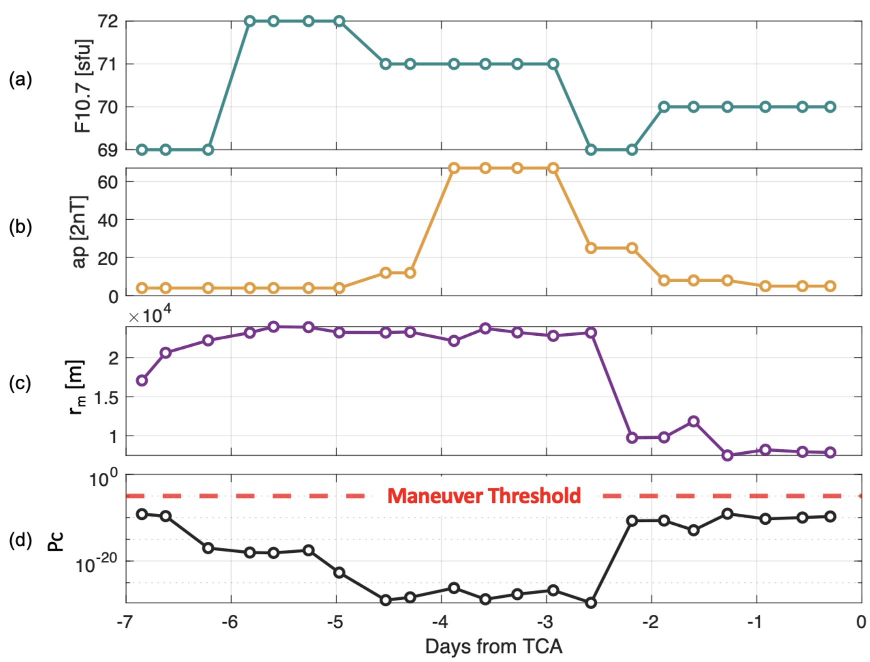

(a)
(b)
(c)
(d)
F10.7 [sfu]
ap [2nT]
r_m [m]
$\times 10^4$
Pc
Maneuver Threshold
Days from TCA

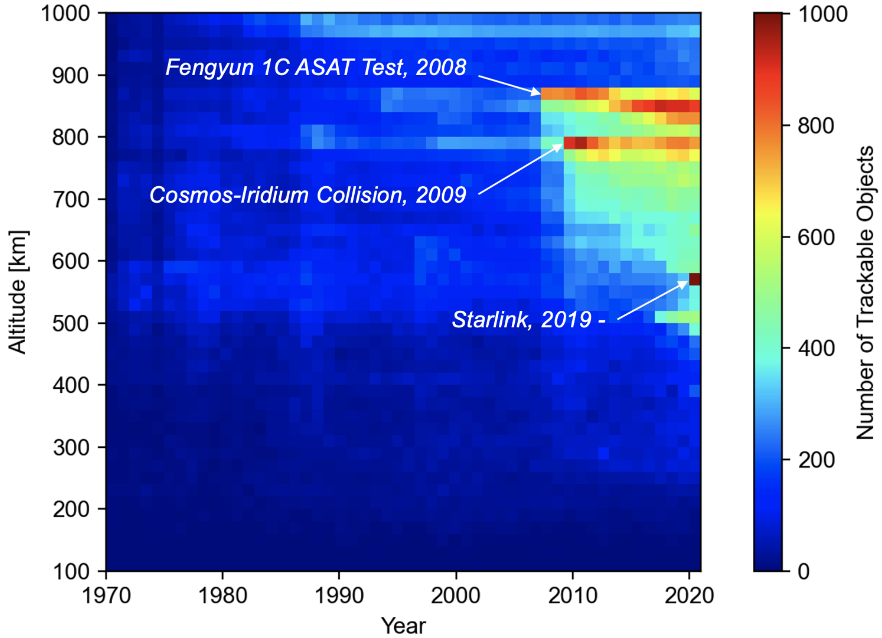
Fengyun 1C ASAT Test, 2008
Cosmos-Iridium Collision, 2009
Starlink, 2019 -
Altitude [km]
Year
Number of Trackable Objects

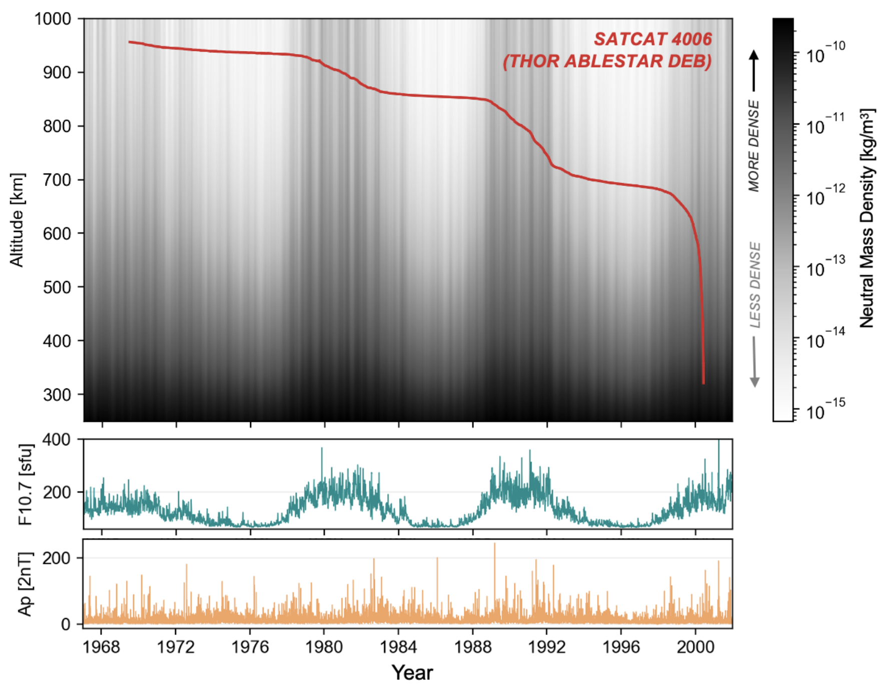
SATCAT 4006
(THOR ABLESTAR DEB)
Altitude [km]
MORE DENSE
LESS DENSE
Neutral Mass Density [kg/m³]
F10.7 [sfu]
Ap [2nT]
Year

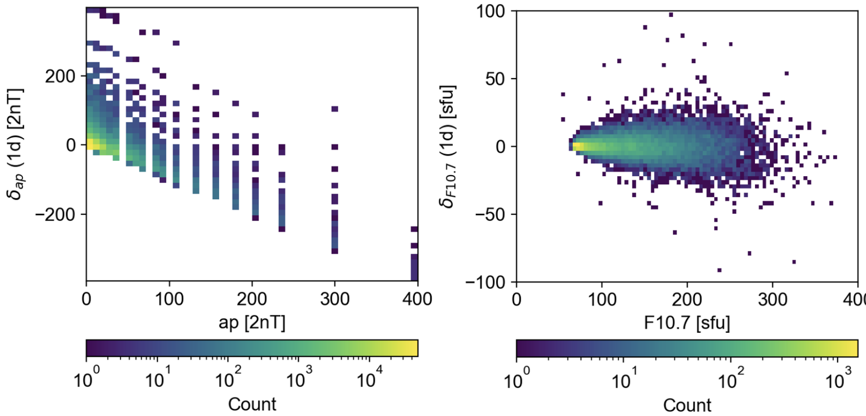

(a) (b)

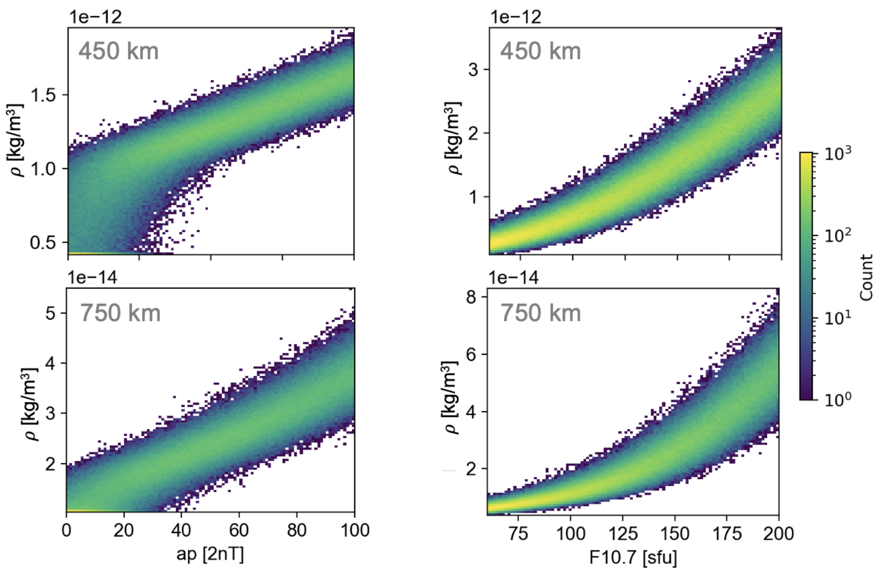

(a)
F10.7 = 120 [sfu]
F10.7A = 120 [sfu]
ap = $\mathcal{N}$(x, 10^2) [2nT]

(b)
F10.7 = $\mathcal{N}$(x, 10^2) [sfu]
F10.7A = x [sfu]
ap = 20 [2nT]

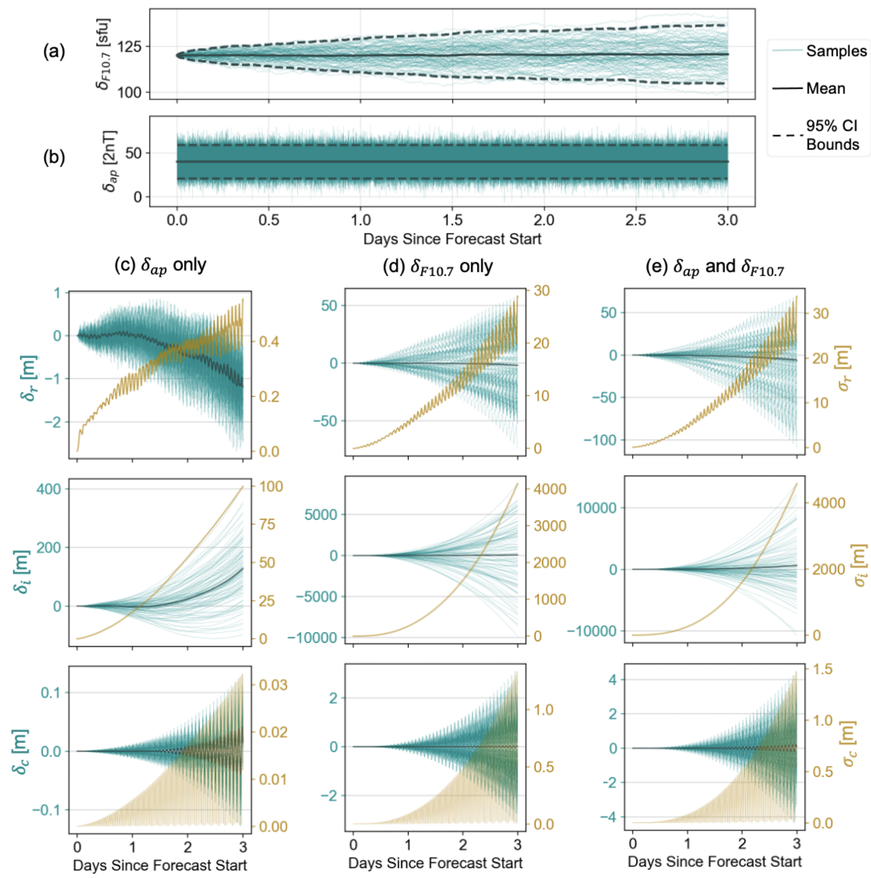
(a)
$\delta_{F10.7}$ [sfu]
(b)
δ_{ap} [2nT]
Samples
Mean
95% CI Bounds
Days Since Forecast Start
(c) δ_{ap} only
(d) $\delta_{F10.7}$ only
(e) δ_{ap} and $\delta_{F10.7}$
δ_r [m]
σ_r [m]
δ_i [m]
σ_i [m]
δ_c [m]
σ_c [m]
Days Since Forecast Start
Days Since Forecast Start
Days Since Forecast Start

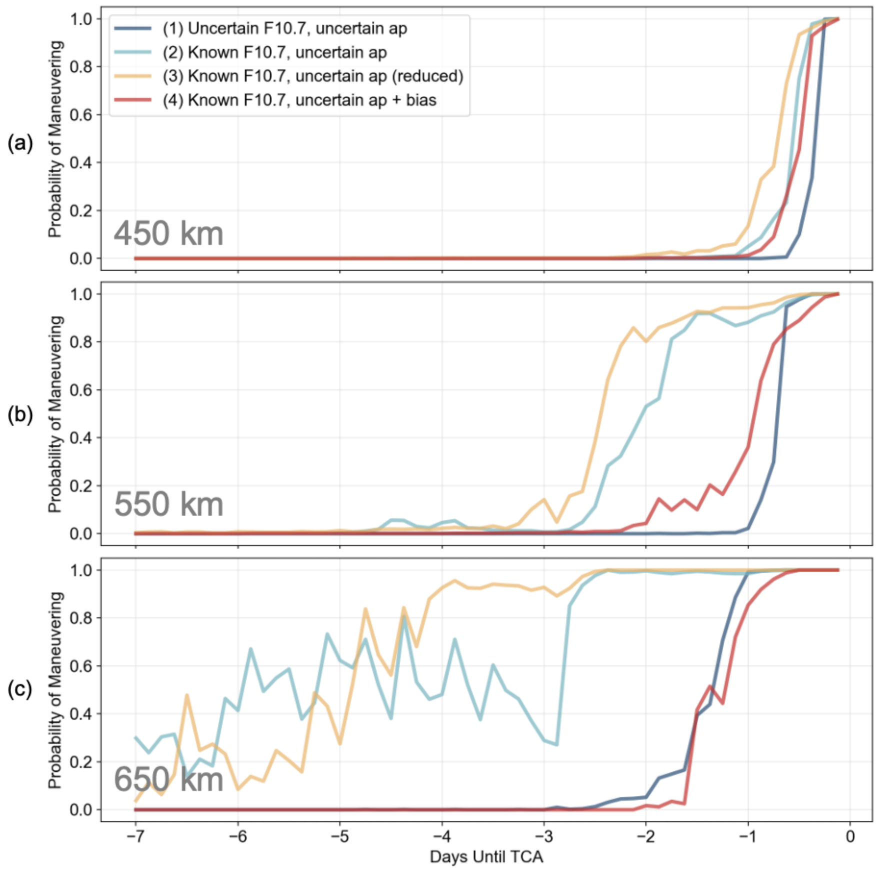
(1) Uncertain F10.7, uncertain ap
(2) Known F10.7, uncertain ap
(3) Known F10.7, uncertain ap (reduced)
(4) Known F10.7, uncertain ap + bias
(a)
(b)
(c)
450 km
550 km
650 km
Probability of Maneuvering
Days Until TCA

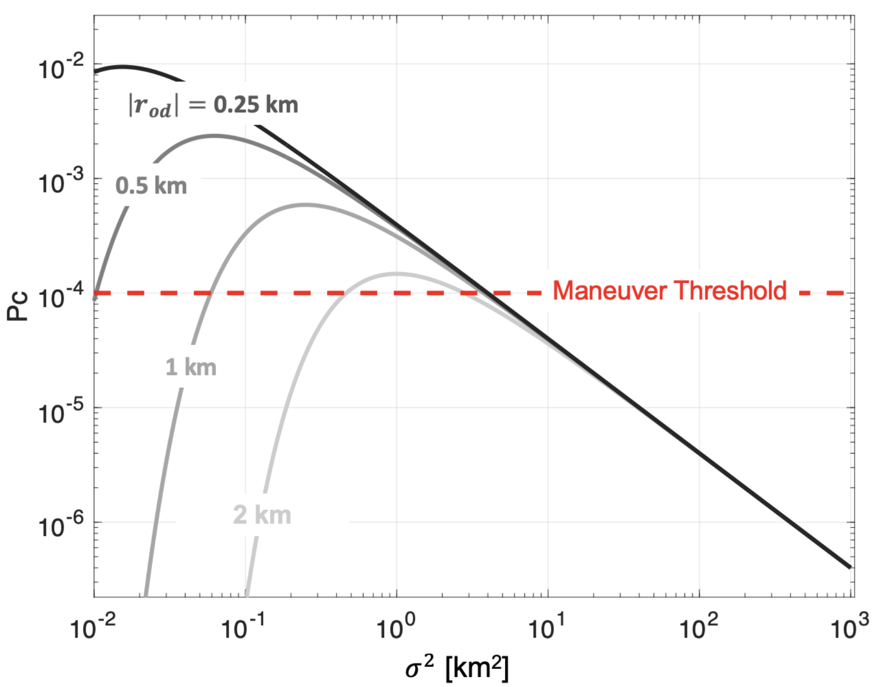
$|r_{od}|$ = 0.25 km
0.5 km
1 km
2 km
Maneuver Threshold
Pc
σ^2 [km^2]

Influences of Space Weather Forecasting Uncertainty on Satellite Conjunction Assessment

William E. Parker[1], Mervyn Freeman[2], Gareth Chisham[2], Andrew Kavanagh[2], Peng Mun Siew[1], Victor Rodriguez-Fernandez[3], Richard Linares[1]

[1]Massachusetts Institute of Technology, Cambridge, Massachusetts 02139
[2]British Antarctic Survey, Cambridge, United Kingdom, CB3 0ET
[3]Universidad Politécnica de Madrid, Madrid, Spain 28040

Key Points:

- Poor forecasts of space weather indices inhibit our ability to perform actionable satellite conjunction assessment with advance notice.
- Uncertainty in the space weather index forecast is translated into uncertainty in position in the satellite body-fixed frame.
- Example scenarios show that accurate, uncertainty-aware space weather index forecasts can help make better maneuver decisions sooner.

Corresponding author: William E. Parker, `wparker@mit.edu`

Abstract

A significant increase in the number of anthropogenic objects in Earth orbit has necessitated the development of satellite conjunction assessment and collision avoidance capabilities for new spacecraft. Often, the greatest source of uncertainty in predicting a satellite's trajectory in low Earth orbit originates from atmospheric neutral mass density variability caused by enhanced geomagnetic activity and solar EUV absorption. This work investigates the impacts of solar and geomagnetic index forecasting uncertainty on satellite drag and satellite maneuver decision-making. During an averaged point in the solar cycle, accurate index forecasts with reduced uncertainty are shown to provide significantly improved advance notice for dangerous conjunction events above 500 km. Below 500 km, forecast improvements are less impactful. This boundary of utility from forecast improvements shifts upward and downward during solar maximum and solar minimum, respectively. Improved index forecasts are shown to have little impact on making maneuver decisions 12-24 hours from a potential conjunction event, but are demonstrated to be very useful when trying to make maneuver decisions with more lead time. These improved forecasts of the space weather indices help in making actionable, durable conjunction predictions sooner than is currently possible.

Plain Language Summary

As low earth orbit has become crowded with new satellites and debris, operators have been forced to maneuver satellites to avoid collisions on a regular basis. The drag force on a satellite, which can significantly affect the orbital path, varies depending on solar and geospace activity. Unfortunately, solar activity and resulting effects at Earth are difficult to predict even just a few days in advance. This paper traces space weather forecasting ability directly to impacts on satellite maneuver decision-making, and finds that better forecasts enable good maneuver decisions earlier than is possible with current forecasts.

1 Introduction

Recent rapid growth in the population of active satellites and debris objects in low Earth orbit (LEO) has led to a clear need for satellite conjunction assessment, risk analysis (CARA), and collision avoidance (COLA) maneuvering capability. Today, a space domain awareness ecosystem exists that allows satellite operators to track objects in orbit, predict conjunctions in advance, and make decisions regarding satellite maneuvering to mitigate the risk of a collision. Organizations like the US Space Force's 18^{th} Space Defense Squadron provide conjunction data messages (CDMs) (Consultative Committee for Space Data Systems, 2022) to operators responsible for performing the subsequent risk analysis and making COLA decisions for their assets.

With the advent of proliferated LEO constellations in recent years, CARA tasks are routinely becoming more automated to reduce operator burden. Figure 1 shows the number of tracked objects since 1970 in time-averaged orbit altitude bins. Significant debris-generating events, including the Chinese Fengyun 1C ASAT test in 2008 and the Cosmos-Iridium collision in 2009 are clearly apparent. The subsequent decay of the resulting debris populations from these events is also visible. In 2019, Starlink began operating thousands of satellites around 550 km, where the constellation is subject to constant bombardment from debris falling from breakup events above. Managing such a large constellation in a debris-filled environment requires careful automation and robust procedures for collision avoidance.

Considering this growing automation of CARA and COLA tasks, many operators have developed internal protocols for determining whether a COLA maneuver is appropriate for a conjunction scenario of interest. Most maneuver decisions consider the prob-

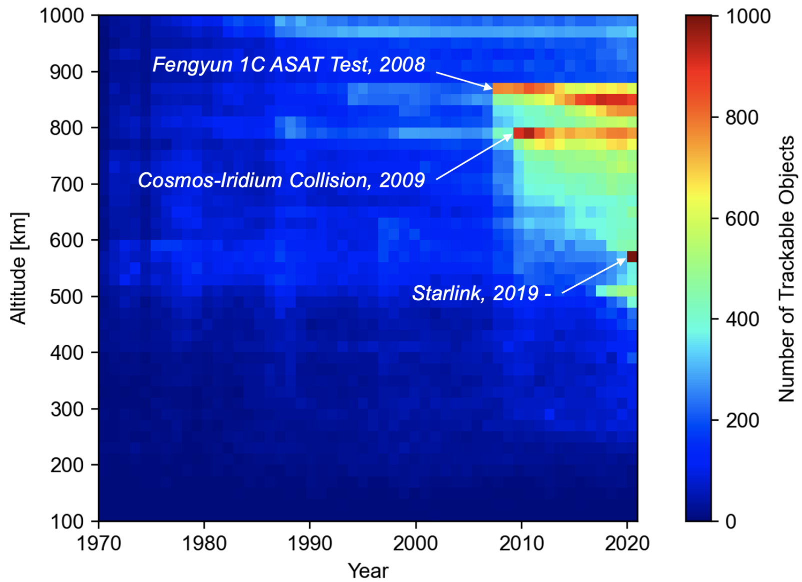

Figure 1. Tracked objects by altitude since 1970, created using a history of two-line element (TLE) data. The 2008 Chinese ASAT test and 2009 Cosmos-Iridium Collision are clearly defined with debris decay following afterwards. The beginning of the Starlink constellation is also visible.

ability of collision (Pc), computed based on imperfect knowledge of the scenario and a model for evolving the states of the objects of interest. While the interpretation of potential conjunction events is probabilistic based on imperfect measurements and models, the potential collision event itself is deterministic. Given perfect observations and a perfect process model, the probability of collision at any time before the conjunction event should be either zero or one. However, uncertainty in measurements and satellite propagation complicates the analysis. As the time until the conjunction event drops, better knowledge of the state of each object from new observations, along with a lower process model error, results in a better understanding of the likely outcome.

Most potential conjunction events are identified during screening about seven days in advance of the time of closest approach (TCA). However, many operators choose to wait until 12-24 hours or less before TCA to decide whether or not to maneuver. This waiting is necessary because there is often significant process error in the state propagation of the objects involved in the conjunction, and updating the states of the objects with recent measurements constrains the growth of this process error.

Operators choose to wait to make maneuver decisions because collision avoidance maneuvers are costly. While the amount of propellant expended for collision avoidance maneuvers is typically small compared to the amount used for station-keeping, such maneuvers can routinely prevent a satellite from performing its desired task (Earth observation, serving users, charging solar panels, communicating with ground stations, etc.) for hours on end. However, many active satellites (especially small satellites) lack propulsion systems capable of performing last-minute COLA maneuvers. Instead, these satellites may often use differential-drag techniques, which can mitigate risk but require several days' notice to be effective. Even for satellites with propulsion systems, it is often inconvenient or impossible to maneuver at a moment's notice since this likely means missed passes of ground targets or communications opportunities. For tracked, non-maneuverable debris objects, laser-nudging may be an effective means of collision avoidance maneuvering (NASA, 2023), but even this approach still requires advance notice exceeding the current standard for operations.

If satellite propagation accuracy and uncertainty are improved, good maneuver decisions could be made sooner with the same level of risk. The following sections discuss limitations in our ability to predict satellite motion in LEO, how these limitations impact the conjunction risk assessment process, and what steps can be taken to make durable collision avoidance maneuver decisions sooner. After a discussion of the uncertainties involved in predicting satellite drag in Section 2, capabilities and limitations in forecasting atmospheric neutral mass density are discussed in Section 3. Then, the probability of collision metric is introduced and a dangerous scenario is highlighted using actual historical CDM data in Section 4. Finally, semi-analytical and numerical methods for translating space weather index uncertainty into satellite state uncertainty are explained in Section 5, which are used for performing simulated conjunction assessment scenarios for collision events in Section 6.

2 Satellite Drag

As the largest contributor to state propagation error in LEO, significant effort has been devoted to improving satellite drag models in recent years. The acceleration due to atmospheric drag on a satellite is computed by

$$\ddot{\mathbf{r}}_D = -\frac{1}{2}\frac{C_d A}{m}\rho v_{rel}^2 \mathbf{e}_{rel}, \tag{1}$$

where $\mathbf{r}$ is the satellite position vector in an Earth-centered inertial frame, ρ is the atmospheric neutral mass density, v_{rel} is the magnitude of the velocity of the satellite relative to the motion of the atmosphere, C_d is the drag coefficient, A is the frontal area of the satellite normal to the direction of motion relative to the atmosphere, m is the mass of the satellite, and $\mathbf{e}_{rel}$ is the unit vector in the direction of satellite relative velocity. In practice, the uncertain C_d, A, and m are often combined as

$$B = \frac{C_d A}{m}, \tag{2}$$

or, in some cases

$$B^* = \frac{C_d A \rho_0}{2m}, \tag{3}$$

where ρ_0 is the reference density of 0.15696615 kg/(m^2·R_E), and R_E is the average Earth radius (Hoots, 1980). It follows that

$$\ddot{\mathbf{r}}_D = -\frac{1}{2}\rho v_{rel}^2 B \mathbf{e}_{rel} = -\frac{\rho}{\rho_0} v_{rel}^2 B^* \mathbf{e}_{rel}. \tag{4}$$

To accurately predict satellite drag (and evolve uncertainty in that prediction), it is prudent to consider each term in Eq. 1 as uncertain. v_{rel} and $\mathbf{e}_{rel}$ are often well characterized during quiet periods because the winds in the upper atmosphere are much lower in magnitude than the spacecraft's velocity. However, geomagnetic disturbances have been shown to produce enhanced neutral winds in the upper atmosphere. The speed of the neutral winds can, at times, approach 1 km/s, which can cause rapid unpredictable fluctuations in apparent velocity for a LEO satellite (Zhang & Shepherd, 2000; Wang et al., 2008). Mass m, exposed frontal area A, and drag coefficient C_d are often very uncertain because these quantities require knowledge of the properties of the object being tracked that cannot be readily estimated directly from remote measurements. The rough size and mass of the object under study have been inferred from past orbital history (Gondelach et al., 2017), measurements of radar cross section (Dickey & Culp, 1989) or visual magnitude (Šilha, 2020). A and C_d are a function of satellite attitude, which is difficult to measure in real-time. Still, light curve measurements have been used to better characterize the attitude dynamics for tumbling objects of interest (Linares et al., 2014; Schildknecht et al., 2017; Šilha et al., 2018). This knowledge of satellite attitude dynamics can be helpful for understanding and predicting how C_d and A vary in time. However, most previous efforts at improving drag models have focused on estimating the combined term B or B^* instead of inferring each parameter individually (Bowman, 2002; Saunders et al., 2012; Gondelach et al., 2017).

In an analysis of satellite drag forecasting error during one month of observations, Hejduk and Snow (M. D. Hejduk & Snow, 2018) found that uncertainty in atmospheric density outweighed uncertainty in B 92% of the time. This makes sense, considering that variability in neutral mass density is common on both long and short timescales due to solar EUV radiation and Joule heating, respectively. Because satellite decay is so strongly influenced by solar and geomagnetic activity, significant effort has been devoted to developing improved space weather models and observation techniques to reduce the uncertainty that arises due to this extreme variability in neutral mass density.

Error in density forecasts can be attributed to either error in the predicted space weather model inputs or error in the models themselves. When focusing on errors in the space weather inputs, Bussy-Virat et al. (Bussy-Virat et al., 2018) found that accounting for uncertainties in projected $F10.7$ and A_p in the per-object covariances at TCA can lead to significantly different estimates of Pc . When considering error in the neutral mass density models, Hejduk and Snow (M. D. Hejduk & Snow, 2019) found that ignoring model uncertainty can cause dangerous conjunction events to go unnoticed. Gondelach et al. (2022) also quantified and propagated model uncertainty, but included a correlation factor between the position uncertainties of the two objects involved in the conjunction. This correlation recognizes the idea that, often, both objects involved in a conjunction will travel through similar perturbed regions of the atmosphere. In general, the goal of all of this work in uncertainty quantification is to accurately represent the true uncertainty in the predicted state of the objects being tracked based on the information available at the time of the estimate. This covariance-realism effort ensures that maneuver decisions are made based on accurate projected uncertainties, and is of much interest to the space surveillance and tracking community (Aristoff et al., 2016).

3 Forecasting Neutral Mass Density

Variability in neutral density within the thermosphere is driven largely by the absorption of solar radiation in the XUV, EUV, and FUV ranges as well as Joule heating during periods of enhanced geomagnetic activity. Many models of the upper atmosphere rely on space weather indices as inputs to describe these dynamics. The indices help to simplify complex information about the solar or geospace environment into a set of scalar variables. One space weather index of particular interest is *F10.7*, the solar radio flux at 10.7 cm, because it has been observed to be correlated with solar EUV flux (Covington, 1948; Tapping, 2013; Picone et al., 2002). The 81-day average of the index, $F10.7A$, is also sometimes used as an input for models. A major geomagnetic index of interest is Ap, which is derived from the Kp index and is computed by combining measurements of Earth's magnetic field from thirteen specific observatories around the world (Bartels, 1949). Ap is the daily average value of the index ap, which is computed every three hours. These geomagnetic indices help to estimate the rapid enhancements in neutral density in the thermosphere associated with Joule heating.

Figure 2 shows the passive orbital decay of SATCAT 4006, a debris fragment from the Thor-Ablestar breakup event of 1961, over its tracked lifetime with historical globally-averaged neutral mass density from (J. Emmert et al., 2021) plotted in the background. The history of satellite altitude was extracted from tracking data in the form of two-line orbital element (TLE) sets for the object. The satellite path clearly shows higher rates of decay during solar maximum (high $F10.7$) than during solar minimum (low $F10.7$). Small deviations in decay rate, mostly visible during solar maximum, are from rapid density enhancements caused by increased geomagnetic activity.

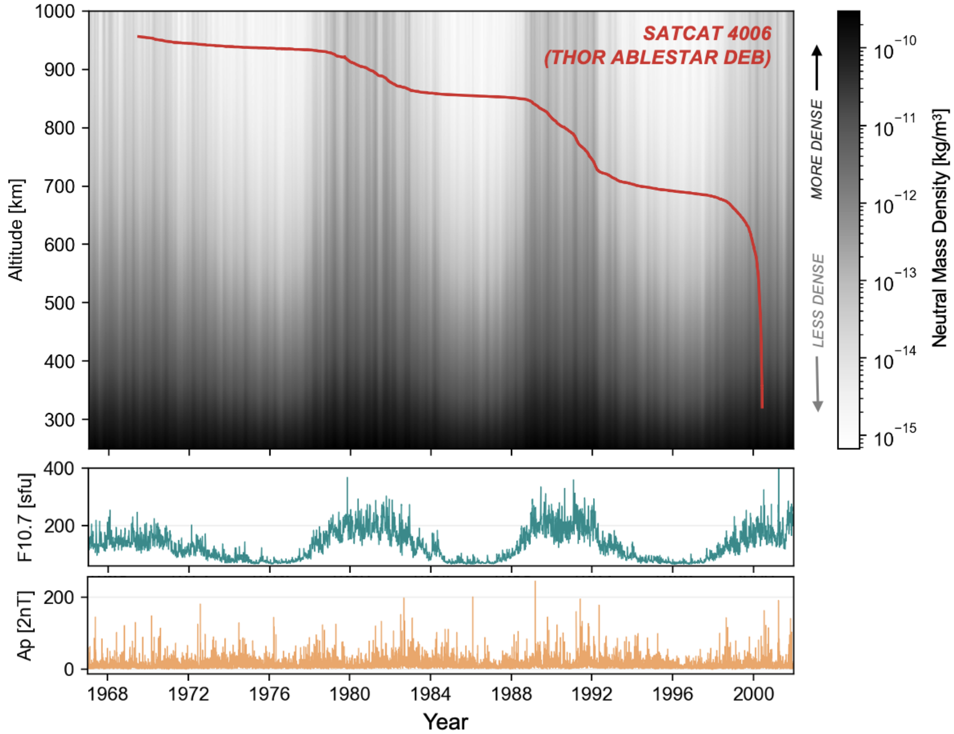

Figure 2. Passive decay of SATCAT 4006 (Thor Ablestar Debris) through multiple solar cycles, with altitude and time-resolved neutral mass density estimates shown in the background for reference. Below, a history of $F10.7$ and Ap are correlated with the density trends observed over time.

Several empirical and physics-based models for the dynamics of the thermosphere-ionosphere system have been developed over the years. Recent *in situ* measurements of thermosphere density and temperature from satellite missions like CHAMP (Reigber et al., 1999), GRACE (Davis et al., 2000), and Swarm (Doornbos et al., 2009) have provided excellent, while sparse, observations to compare model performance to under a variety of conditions. While significant progress has been made in modeling the response of the neutral thermosphere to enhanced geomagnetic activity, forecasts of the space weather indices that drive the models have not been comparably improved. These poor forecasts of the space weather indices are often the dominant source of uncertainty in predicting satellite drag.

Recent work in (Licata et al., 2020) benchmarked the performance of operational forecasting models for key space weather drivers like $F10.7$ and Ap, among others. Such forecasts are typically driven by a combination of historical trends in the index under study and a set of current related observations at the forecast time. *Recurrence* and *persistence* are two important principles for these forecasts. Recurrence considers previous observations at interval solar rotations backward in time, while persistence uses the last known value as the best guess for future values of the index. $F10.7$ forecasts can be improved beyond the recurrence or persistence models by supplementing EUV radiation observations from the east limb of the sun or a modeled nowcast of the Sun's surface magnetic field (Lean et al., 2009; Henney et al., 2012, 2015).

Forecasts of geomagnetic indices like Kp and its derived Ap are typically driven by a combination of solar wind measurements at the L1 Lagrange point and a history of measurements for the index. Since measurements of solar wind at L1 provide very little advance notice of what is to arrive at Earth, forecasts of these indices typically have a short useful horizon time. Shprits et al. (2019) found that forecasts for Kp are only reliably accurate for a time horizon of 6 to 20 hours, depending on the solar cycle. Beyond 1-2 days out, forecasts based on recurrence or persistence generally produce the best results (though performance is still quite poor). The skill of a forecast model can be represented by

$$skill = 1 - \frac{RMSE}{\sigma_x}, \tag{5}$$

where, considering N samples with true values $\mathbf{x}$ and estimated values $\hat{\mathbf{x}}$,

$$RMSE = \sqrt{\frac{\Sigma_{i=1}^{N}(x_i - \hat{x}_i)^2}{N}} \tag{6}$$

and

$$\sigma_x = \sqrt{\frac{\Sigma_{i=1}^{N}(x_i - \mu)^2}{N}}. \tag{7}$$

A skill score of 1 corresponds to a perfect forecast and 0 corresponds to a forecast where the RMSE is equal to the standard deviation of the observations. The skill can also be negative if the error in the forecast is larger than the variability in the data it's trying to predict. A good forecast should have a skill score as high as possible.

Figure 3 shows the skill of a NOAA Space Weather Prediction Center (SWPC) Ap forecast as a function of time (using a 5-year rolling average to reduce noise and make general trends apparent). This forecast model was developed in 2014 and then verified on historical data (https://www.swpc.noaa.gov/content/geomagnetic-activity-forecast-verification). The forecasts are separated by their time horizon from 1-7 days, and a plot of the monthly average sunspot number is overlaid. The overall skill of the model is quite low over all time periods. Only the 1-day forecast sits reliably above zero, and the 2-7 day forecasts all appear to have a comparable lack of skill. On close inspection, it appears that the maximum in forecast skill occurs during the declining phase of the previous solar maximum. This improvement in geomagnetic index forecasting can likely be attributed to the elevated coherence in the IMF that generally occurs during this decline in the solar cycle. It is unfortunate that the Ap forecast skill is lowest during solar maximum since this is the period when geomagnetic enhancements can cause the largest changes in atmospheric neutral mass density.

Since ap forecasts are generally poor beyond a time horizon of a few hours to perhaps a day (depending on the state of the solar cycle), and since forecast skill appears from Figure 3 to be relatively constant with forecast time horizon, it is reasonable to simulate ap forecast uncertainty with a white noise process. Such a process has a Gaussian uncertainty that is constant in time. Some complications arise, however, when we consider that there are strict bounds on what values ap can take. If the actual true value of ap at some point in the future is low and the forecast deviates substantially below that (according to a symmetric white noise process), there may be some probability of achieving a sub-zero ap, which cannot exist. Another complexity to consider is that the mapping of input ap to output density is not necessarily linear, and the combination of a nonlinear transformation and the positivity constraint on ap and density can lead to challenges in modeling uncertainty. Figure 4 shows the deviations in ap and $F10.7$ from truth using a simple persistence-based 1-day forecast over all recorded history for the indices from 1957-2023 from the Hemholtz center at GFZ Potsdam. Figure 4a shows that ap forecasts are very much *heteroscedastic* with respect to the mean forecast. Both the spread and the distribution of the forecast uncertainty are clearly a function of the expected value of ap, with very skewed distributions around low forecasted values of ap. Figure 4b shows that the $F10.7$ forecast is also heteroscedastic (though less so than Ap), where uncertainty in the forecast is a function of the expected value of the index.

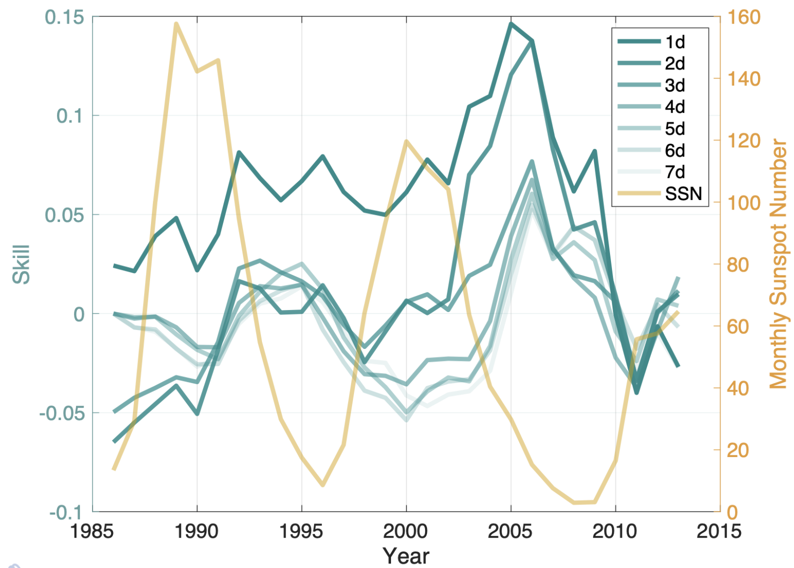

Figure 3. 5-year rolling-average skill of SWPC *Ap* forecasts (from 2014 model verification) by time horizon from 1985-2013. Overlaid is the average monthly sunspot number by year. Forecast skill is low for all time horizons and over all time, but skill appears to improve across all time horizons during the declining phase of the solar cycle.

Figure 5 complicates this scenario further. It shows NRLMSISE-00 modeled density as a function of the input indices, where we assume that uncertainty distributions on the indices are Gaussian (even though Figure 4 shows that this is not always a valid assumption). 5a shows densities computed with input $F10.7 = 120$, $F10.7A = 120$, and $ap = \mathcal{N}(x, 10^2)$, while 5b shows densities from assuming $F10.7 = \mathcal{N}(x, 10^2)$, $F10.7A = x$, and $ap = 20$. For each case, the modeled density is shown for 450 and 750 km altitude. Figure 5a's 450 km case very clearly shows that NRLMSISE-00 modeled density is also heteroscedastic with respect to the mean of the input distribution on ap. Above an input mean of 40, the uncertainty in the output appears relatively constant, but below 40, the distribution in density has much greater spread and no longer appears symmetric (especially considering that input ap cannot drop below zero, so each negative sampled point is assigned an ap of zero). At an altitude of 750 km, uncertainty in ap appears much more consistent across input means. Figure 5b repeats the same analysis, but using an uncertain $F10.7$. Interestingly, uncertainty in modeled density appears to be more heteroscedastic with respect to the mean input $F10.7$ with increasing altitude, opposite from what was observed for ap. Differences in uncertainty over input mean $F10.7$ are much more apparent at 750 km than they are at 450 km.

For the remainder of this work, it is necessary to parameterize the uncertainty in $F10.7$ and Ap as a function of time so that we can modify the uncertainty terms and inspect the influence on maneuver decisions. Even though $F10.7$ and Ap are daily indices (though ap is in 3-hour increments), we shall presume that the indices are continuous and that the atmospheric response to variability in the indices is instantaneous. This allows us to sample the indices according to a probability distribution for each timestep of the satellite propagation. ap will be considered the continuous-time variable for Ap from here forward.

Lacking a reasonable reference ap forecast model with a long history for performance comparison, we shall retain the white noise assumption for the ap forecasts for this work. To limit significant violations of this assumption, the following seconds consider a true

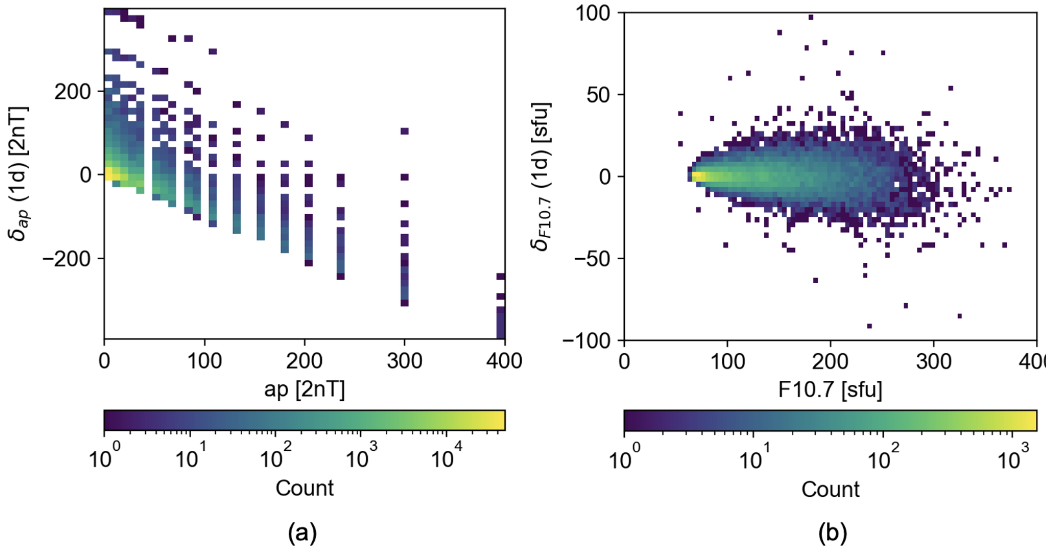

Figure 4. Deviation from 1-day forecasted indices based on a simple persistence model using the historical record. (a) shows the deviation in the three-hour ap (which appears sparse because it is derived from Kp), and (b) shows the deviation in the daily adjusted $F10.7$. Both are heteroscedastic.

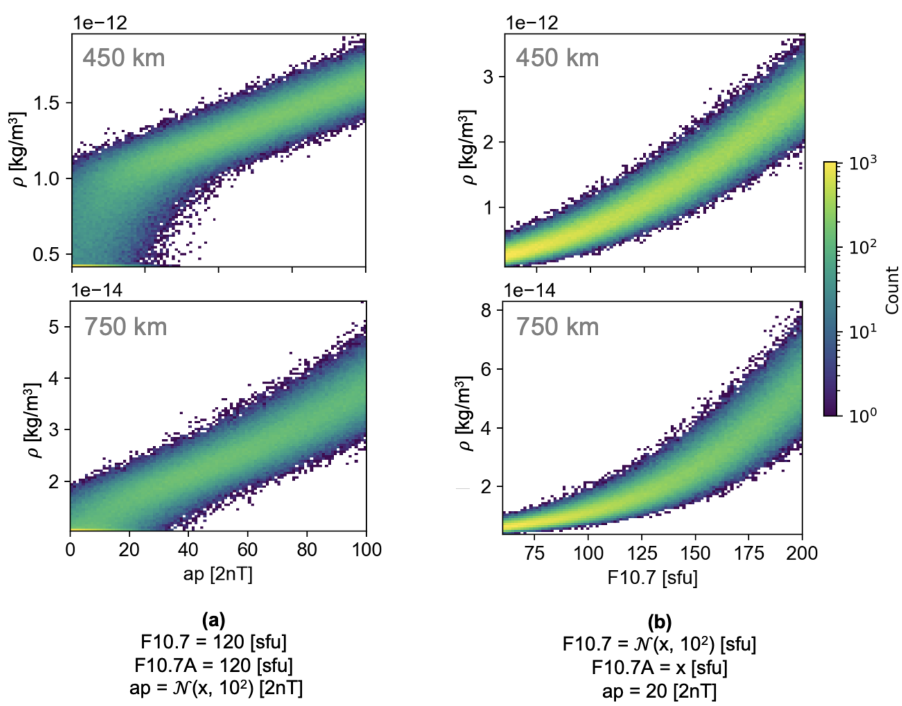

Figure 5. NRLMSISE-00 Densities as computed with Gaussian distributed input uncertainties of (a) $\sigma_{\delta_{ap}} = 10$, (b) $\sigma_{\delta_{F10.7}} = 10$, and means as denoted on the x-axis. 450 and 750 km altitudes are shown to demonstrate how heteroscedasticity for density with respect to the indices changes with altitude.

ap forecast that is 40 $2nT$ or above. Additional effort is required to properly account for uncertainty in density from lower forecasted values of *ap*. If at any time the sampled forecast *ap* falls below zero, it will be replaced with zero. The standard deviation of the white noise process ($\sigma_{\delta ap} = 10$) was selected based on *ap* climatology and a simple persistence model.

J. T. Emmert et al. (2017) found that $F10.7$ forecasts tend to deviate from truth with roughly Brownian motion over time. That assumption will be made here as well. At each timestep, the probability density function of the deviation is Gaussian distributed with mean zero and standard deviation $\sigma_{\delta_{F10.7}}(t) = 0.015\sqrt{t}$, which was determined empirically to match the historical performance of $F10.7$ forecasts from (Licata et al., 2020; J. T. Emmert et al., 2017; Stevenson et al., 2022).

4 Space Weather and Collision Probability

Over the years, several metrics have been proposed and used in an attempt to quantify the risk of a collision between two resident space objects (RSOs). In the early days, a predicted offset distance was the only parameter considered in the conjunction assessment process (Patera, 2001). But as probabilistic projections of satellite state became available, using deterministic offset distances meant leaving probabilistic information on the table. Today, most operators agree that tracking the probability of collision, computed by considering both the predicted offset distance and the evolved state covariances for the objects of interest (as well as their presumed hard body radii), is a prudent approach to conjunction risk assessment. A satellite operator will generally assign a probability of collision maneuver threshold based on a balance of the risks of a collision and the costs of performing too many maneuvers. NASA generally uses a Pc maneuver threshold of 10^{-4} (i.e. a probability of $\frac{1}{10{,}000}$), while SpaceX generally uses a probability threshold of 10^{-5} (or $\frac{1}{100{,}000}$). NASA, however, tends to maneuver 24 hours prior to TCA while SpaceX delays maneuvering until 12 hours or less before TCA, which significantly reduces the maneuver burden (Moomey et al., 2023).

When conjunction relative velocities exceed 1 km/s, it becomes reasonable to assume that motion is rectilinear and that the interaction between objects occurs on a plane in the encounter frame of the conjunction. The probability of collision is then a function of the combined hard body radius of the two objects involved in the conjunction, R, the offset or miss distance in the conjunction plane, r_m (with major and minor axis components x_m and y_m), and the 2-dimensional state covariance in the encounter plane with standard deviation components σ_x and σ_y. Pc is computed by

$$P_c(R, x_m, y_m, \sigma_x, \sigma_y) = \frac{1}{2\pi\sigma_x\sigma_y} \int_{-R}^{R} \int_{-\sqrt{R^2-x^2}}^{\sqrt{R^2-x^2}} e^{-\frac{1}{2}\left[\left(\frac{x-x_{od}}{\sigma_x}\right)^2+\left(\frac{y-y_{od}}{\sigma_y}\right)^2\right]}\, dy\, dx. \tag{8}$$

Different implementations of solvers for the equation above have been developed over the years that have become increasingly computationally efficient and robust, including (Foster & Estes, 1992; Chan, 1997; Patera, 2001), and (Alfano, 2005). More information about computing a 2D probability of collision can be found in (Alfano, 2007).

Figure 6 shows that for a conjunction scenario of interest, there are two possible ways to achieve a low Pc. The right side of the Pc maximum for each curve is called the *dilution region*. It is impossible to achieve a high probability when position uncertainty at TCA is large. Reducing the covariance size (i.e. making better observations and having better predictions) in the diluted region leads to an increase in the Pc. To the left of each maximum is what is referred to as the *robust region*. Pc is low here when the predicted offset distance is much larger than the uncertainty in object positions. Decreasing covariance size in the robust region leads to a reduction in Pc.

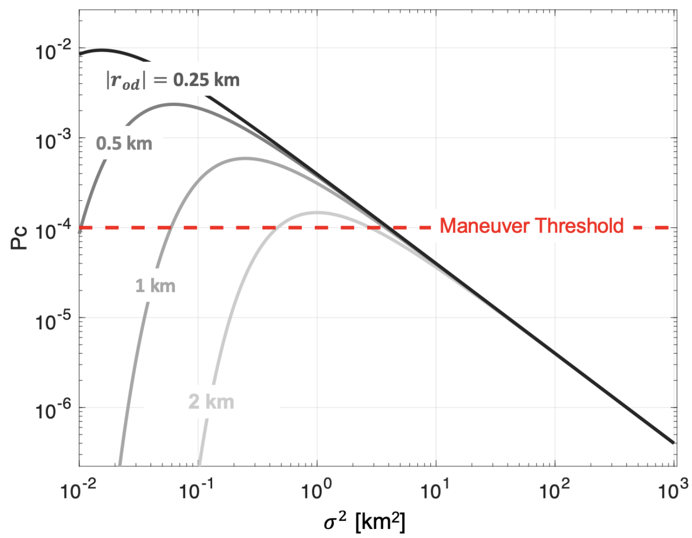

Figure 6. Probability of collision as a function of the position variance and predicted offset distance at TCA. Regions to the right of maximum Pc are considered *diluted*, and maneuver decisions cannot be reliably made here. Increasing the offset distance has the effect of reducing the maximum Pc and pushing this maximum further to the right.

It is always preferred to exist within the robust region. When in this region, operators are generally confident about their computed Pc and have reason to believe that improved measurements should reduce Pc as time goes on. The figure demonstrates that the ratio of the offset distance to the covariance size is important in determining when the transition into the robust region will take place. Conjunctions with a small offset distance take longer to reach the robust region, while conjunctions that end in a collision will never enter the robust region. This analysis is critically dependent on accurate estimates of the offset distance, $\hat{r}_m$ between the objects at TCA, yet $\hat{r}_m$ often varies quite considerably in time when forecasted drag deviates from truth.

To better understand the impact that poor space weather forecast models can have on Pc, a history of real CDMs is useful. In 2019, a set of CDMs was publicly released as part of an ESA conjunction assessment challenge (Uriot et al., 2022). An example conjunction from this dataset with some of its CDM parameters and relevant space weather indices is shown in Figure 7. Figure 7a shows the $F10.7$ index as recorded for the dates of the CDMs in the conjunction. These values of F10.7 are quite low and relatively stable with no large enhancements or fluctuations. Figure 7b shows the ap index values recorded during the conjunction assessment period. The enhancement in ap from $TCA{-}5\ d$ to $TCA - 2\ d$ would be expected to lead to increased Joule heating and neutral density enhancements, which could lead to increased drag on the propagated objects. Figure 7c shows the predicted offset distance from each CDM. Prior to the period of enhanced ap, the offset distance is predicted to be large. After seeing increased drag during the period of enhanced geomagnetic activity, however, there is a large drop in the predicted offset distance – making a collision suddenly appear much more likely. If the storm was predicted well, a sudden change in the predicted offset distance wouldn't occur. Figure 7d shows the computed probability of collision for each CDM in the conjunction chain. The Pc plot initially shows steady declines in Pc as covariance drops with more recent measurements, as expected. Then, when the predicted offset distance drops suddenly following the storm, it is accompanied by a sudden increase in the predicted Pc. While Pc in this case is below the thresholds for maneuvering, major fluctuations in the predicted

Pc when close to TCA are problematic since they complicate the maneuver decision-making process. This conjunction series demonstrates the problems that arise when space weather forecasts are not accurate or considered in the conjunction assessment process. Improving space weather forecasts and the way that they are handled in conjunction assessment is critical for protecting against events like this. Otherwise, the capabilities of the entire conjunction assessment pipeline will remain diminished during periods of geomagnetic storms and other intervals of enhanced geomagnetic activity.

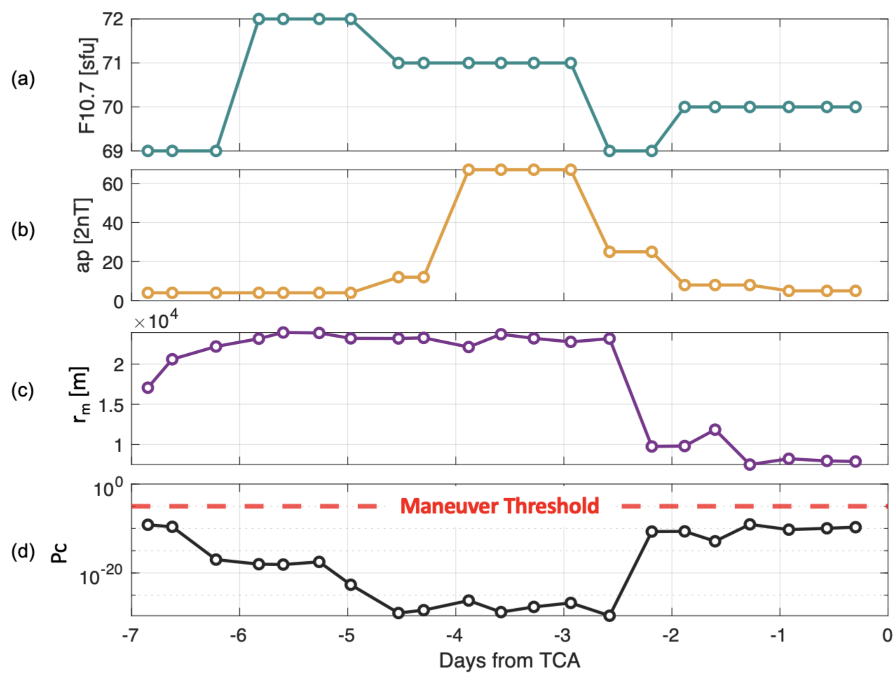

Figure 7. Parameters of interest from a real set of CDMs belonging to a conjunction of interest. (a) shows $F10.7$ at the time each CDM was generated, (b) shows the three-hour ap index, (c) shows the predicted offset distance from each CDM, and (d) shows the resulting Pc over time. Large jumps in Pc can likely be attributed to poor forecasting of the geomagnetic enhancement apparent in ap between $TCA - 5d$ and $TCA - 2d$.

5 Incorporating Index Forecasts into Propagated Uncertainty

Various approaches have been implemented in practice to propagate spacecraft state uncertainty considering the influences of space weather effects throughout the propagation. Most operational methods feed the forecasted space weather indices through a simple empirical model for neutral density. This nominal density profile is then used to propagate the state of the spacecraft. Clearly, there is some uncertainty in the model and in the forecast that needs to be accounted for in this propagation in order to accurately represent the satellite state covariance at the time of closest approach. In practice, this uncertainty quantification is often performed by again employing an empirical model that considers historical error in neutral mass density predictions as a function of the space weather conditions (i.e. during quiet, moderate, or storm-time environments). Uncertainty in the density is then captured in the propagation by adding a "consider parameter" that artificially inflates uncertainty in the B^* term, which will impact overall satellite state uncertainty (M. Hejduk, 2019; Poore et al., 2016; Barker et al., 2000). One problem with this approach is that it combines the contributions of ballistic coefficient uncertainty and atmospheric uncertainty, which makes analysis of uncertainty difficult. Ideally, uncertainty in atmospheric density, and thus propagated satellite state, should be derived analytically from its root causes – uncertainty in the forecasted space weather indices and uncertainty in the atmospheric model.

Drag influences the mean motion of a satellite's orbit by

$$\dot{n} = \frac{3}{2} n^{1/3} \mu^{-2/3} \rho B v^3 F \tag{9}$$

where $n = \sqrt{\mu/a^3}$ is the mean motion, a is the semi-major axis, μ is the gravitational parameter, ρ is the neutral mass density, v is the orbital speed, and F is a factor based on the thermospheric winds:

$$F = \frac{\|\mathbf{v} - \mathbf{v}_A\|^2}{v^2} \mathbf{e_v} \cdot \mathbf{e_{v-v_A}} \tag{10}$$

where $\mathbf{v}$ is satellite velocity, $\mathbf{v}_A$ is the velocity of the atmosphere, and $\mathbf{e_v}$ and $\mathbf{e_{v-v_A}}$ are unit vectors in the subscribed vector directions. The mean anomaly may be computed from mean motion by

$$\frac{dM}{dt} = n. \tag{11}$$

J. T. Emmert et al. (2017) derived the following analytical expressions for the deviation in the n and M as a function of the relative neutral density error, ϵ_ρ along the orbital path:

$$\delta_n(t) \approx \delta_{n_0} \left(1 + \frac{1}{3}\frac{\Delta\hat{n}}{\Delta\hat{n}_0}\right) + \frac{\Delta\hat{n}}{\Delta t} \int_{t_0}^{t} \epsilon_\rho(t')dt' \tag{12}$$

$$\delta_M(t) \approx \delta_{M_0} + \delta_{n_0}\Delta t \left(1 + \frac{1}{6}\frac{\Delta\hat{n}}{\hat{n}_0}\right) + \frac{\Delta\hat{n}}{\Delta t} \int_{t_0}^{t} \int_{t_0}^{t'} \epsilon_\rho(t'')dt''dt' \tag{13}$$

where δ_{n_0} and δ_{M_0} are the initial measurement errors for the mean motion and mean anomaly, respectively. The relative error is defined as

$$\epsilon_\rho(t) = \frac{\hat{\rho}(t) - \rho(t)}{\rho(t)}. \tag{14}$$

We define $n_{ref}(t)$ and $M_{ref}(t)$ as the reference values in n and M using the true density. Thus $\epsilon_\rho = 0$ for the reference case. $n_{ref}(t)$ and $M_{ref}(t)$ may be computed by numerical propagation through the real atmospheric density profile along the orbital path. When starting from perfectly known n and M, Equations 12 and 13 show that error over time in n is proportional to the first integral of the normalized density error, while error in M is proportional to the second integral of the normalized density error. For Pc computation, however, we are interested in deviations in the spacecraft-fixed frame defined by the radial, in-track, and cross-track (RIC) components $(\delta_r, \delta_i, \delta_c)$. The unit vectors for this coordinate frame may be computed from an Earth-centered inertial position $\mathbf{r}$ and velocity $\mathbf{v}$ where

$$\mathbf{e}_r = \frac{\mathbf{r}}{\|\mathbf{r}\|},\ \mathbf{e}_i = \frac{\mathbf{v}}{\|\mathbf{v}\|},\ \mathbf{e}_c = \frac{\mathbf{r}\times\mathbf{v}}{\|\mathbf{r}\times\mathbf{v}\|}. \tag{15}$$

An approximate conversion from δ_n and δ_M to δ_r and δ_i, respectively, is relatively straightforward from Keplerian dynamics. For position errors that are small relative to the curvature of the orbit path, the radial component of the deviation relates to a change in the semi-major axis of the ellipse, the along-track component relates to the deviation in true anomaly. The normal component relates to small plane changes that occur when the right ascension of the ascending node (RAAN, Ω) drifts at slightly different rates as the semi-major axis changes throughout the propagation. This nodal drift may be approximated using J_2 perturbations.

Using Earth's gravitational parameter $\mu = 398600\ km^3/s^2$, the semi-major axis of the orbit may be computed from $n(t) = n_0 + \delta_n(t)$ directly

$$a(t) = \left(\frac{\mu}{(n(t))^2}\right)^{1/3}. \tag{16}$$

The eccentric anomally can be solved for numerically from $M(t) = M_0 + \delta_M(t)$ by the following relation:

$$M(t) = E(t) - e\sin(E(t)) \tag{17}$$

Once $a(t)$ and $E(t)$ are known, the radial distance along the deviated orbit path is simply

$$r(t) = a(t)\left(1 - e\cos(E(t))\right), \tag{18}$$

where e is the eccentricity of the orbit. To determine the deviation in position along the radial component from the reference state, simply compute $\delta_r = r_{dev}(t) - r_{ref}(t)$, where r_{ref} is the radius computed using n_{ref} and M_{ref} with true atmospheric density, while r_{dev} is computed using the deviated density profile.

The along-track satellite position offset, δ_T, is more simply related to the deviation in mean anomaly by

$$\delta_i(t) \approx \delta_M(t)\frac{\hat{v}(t)}{\hat{n}(t)}. \tag{19}$$

Now that the radial and along-track components of the deviation are known, the normal component may be approximated by considering the precession rate of the right ascension of the ascending node, $\dot{\Omega}$, due to J_2 perturbations

$$\dot{\Omega} = -\frac{3}{2}J_2\left(\frac{R_E}{a(1-e^2)}\right)^2\sqrt{\frac{\mu}{a^3}}\cos i \tag{20}$$

where J_2 is Earth's J_2 parameter, R_E is the radius of the Earth, and i is the inclination of the orbit (Vallado, 2001). The inclination is constant, and since the forecasted satellite propagations required for conjunction assessment typically have less than a 7-day time horizon, it is reasonable to approximate the eccentricity as constant as well. Now, a is the only time-varying parameter that $\dot{\Omega}$ depends on. As small changes in a occur during the orbital propagation, differences in the nodal drift rate will accumulate to cause minor shifts in the orbital plane. This out-of-plane perturbation leads to position deviation in the cross-track component, δ_c. We can approximate δ_c by first considering the angle δ_Ω between the orbit planes

$$\delta_\Omega(t) = \int_0^t \left(\dot{\Omega}_{dev} - \dot{\Omega}_{ref}\right) t' dt'. \tag{21}$$

Then, the position deviation in the cross-track component is approximately bounded by

$$\|\delta_c(t)\| < 2\bar{a}_{ref}(1+e)\sin(\delta_\Omega(t)). \tag{22}$$

This is a bound because deviation along the normal component will oscillate as a function of time since the deviated and reference orbital planes intersect to cause two crossings along the orbital path.

Figure 8 shows numerically-propagated position deviations in the radial, along-track, and normal component for an object with $B = 0.02\ m^2/kg$, initial altitude of 450 km, eccentricity of zero, and inclination of 80°. 100 sample trajectories were run from the same initial starting point using uncertain forecasts of ap and $F10.7$, as shown in Figures 8a and b. For simplicity, the true values for the indices are a constant $ap = 40$ and $F10.7 = 120$ for the duration of these runs. The first column, 8c, shows the deviations in positions from a forecast where only ap is uncertain. The magnitude of the position deviation is much larger in the along-track component than in the radial component, which is also much larger than the deviation in the normal component. This makes sense, since Equations 12 and 13 suggested that along-track error would grow proportionally to the integral of the normalized forecast density error, and that the radial component would grow proportionally to the double-integral of the forecast density error. The normal component deviation is small becuase it is driven by a slow plane-change, and indeed it oscillates between bounds as was predicted. A slight bias is apparent in the radial and along-track components. This bias can be attributed to the slight skewness in the density distribution that occurs when provided an ap around 40 2nT with Gaussian uncertainty at 450 km, as is visible in Figure 5.

Figure 8d shows the deviations along the orbital path when there is only uncertainty in the forecasted $F10.7$. While the relative magnitudes of the deviations between the components remain similar to what was found in 8c, the actual magnitudes are much larger, which makes sense considering that EUV absorption is the primary driver of atmospheric variability. There is very little bias apparent in the F10.7 error-only case, which makes sense since the distribution around the forecasted density provided a Gaussian input F10.7 appears to be symmetric in Figure 5. Figure 8e shows the combined effect of forecast uncertainty in both ap and $F10.7$. Since the magnitude of deviations in the $F10.7$-deviated case significantly outweighs those from the ap-deviated case, the distributions look similar in Figure 8e as they do in Figure 8d. This suggests that at least for cases when the mean forecast is perfect, uncertainty in $F10.7$ plays a far more significant role in determining satellite position uncertainty than does uncertainty in forecasted ap.

6 Simulation Results

In order to persuade a satellite operator or tracking service to adopt new satellite drag forecasting procedures, it's crucial to showcase the complete process, starting from index uncertainty, through to modeled density uncertainty, satellite state uncertainty, and ultimately to the impact on the computed probability of collision and thus decision-making. To simulate an informative set of scenarios, a starting satellite state is initialized for a circular orbit at 450, 550, and 650 km initial altitude, all with an inclination of 80 degrees. The space weather environment is set again to a constant $F10.7 = 120$ (an average value between solar minimum and maximum), $F10.7A = 120$, and $ap = 40$ for the duration of the 7-day simulation. In reality, such a prolonged period of enhanced geomagnetic activity is unlikely, but the highly non-Gaussian and asymmetric distribution of modeled density produced by an ap estimate below 40 with Gaussian uncertainty provides significant complications. Incorporating this modeling of uncertainty for low ap is a valuable topic of future work.

Starting at the initial time, 50 sample objects with perfect initial state knowledge are propagated with accelerations from simple two-body gravitation, atmospheric drag, and J2 Earth oblateness included. The atmospheric density profile that each object travels through is computed by sampling deviations on $F10.7$ and ap using the same processes and uncertainties as Figure 8a and b. A reference object is also propagated us-

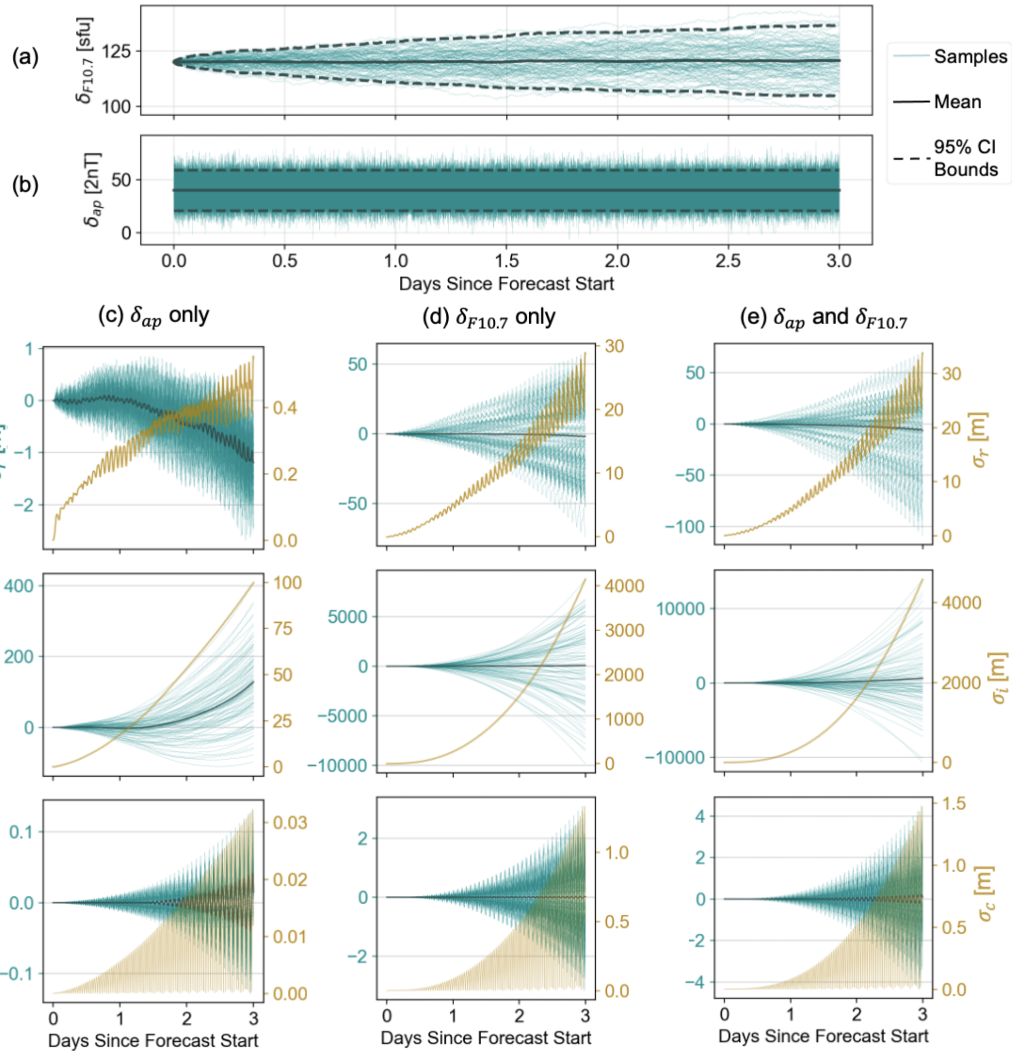

Figure 8. Deviations from a reference "truth" state for (a) $F10.7$, (b) ap, (c) RIC position errors considering only δ_{ap}, (d) RIC position errors considering only $\delta_{F10.7}$, and (e) RIC position errors showing the combined effect of both $\delta_{F10.7}$ and δ_{ap}.

ing the true space weather indices during this period. At 3 hour intervals, a new set of propagated objects are initialized at the location of the reference point for each step. This process simulates taking new measurements every three hours that constrain state uncertainty at that time to zero. The expected state and covariance at TCA for each iteration will differ because the first iteration will have been propagated for 7 days, the second for 6 days 21 hours, and so on. The probability of collision at TCA is computed based on these expected states and covariances, which allows us to compare the computed probability of collision as a function of time until TCA under a variety of circumstances. Four cases are simulated:

- **Case (1)** uses realistic growth in uncertainty for $F10.7$ and ap, as is shown in Figure 8a and b. $F10.7$ deviation is modeled as a Brownian process where $\sigma_{\delta_{F10.7}}(t) = 0.015\sqrt{t}$ (the reference forecasting ability). ap is modeled as a white noise process with $\mu_{\delta_{ap}} = 0$ and a constant $\sigma_{\delta_{ap}} = 10\ 2nT$.

- **Case (2)** assumes that values for $F10.7$ are known at all times throughout the propagation, while uncertainty in ap is still a white noise process with $\mu_{\delta_{ap}} = 0$ and $\sigma_{\delta_{ap}} = 10\ 2nT$.
- **Case (3)** again assumes that $F10.7$ is known, but now uncertainty in ap is reduced with $\sigma_{\delta_{ap}} = 5\ 2nT$.
- **Case (4)** again assumes that F10.7 is known, uses the initial ap uncertainty with $\sigma_{\delta_{ap}} = 10\ 2nT$, but also introduces a $+5\ 2nT$ bias in ap.

To simulate a real event, each of these cases is used to propagate an object from each initialization time to TCA, which provides a set of covariance matrices at TCA as a function of time and case. To emphasize a critical scenario, we simulate a true collision where the primary object (being tracked) and secondary object have a true final centroid offset, $r_{od} = [1, 1, 1][m]$ and each object involved in the conjunction has a hard body radius of 10 m. Such a small centroid offset for a combined hard body radius of 20 m means that this collision will occur.

The velocity of the secondary object relative to the primary object can play an impactful role in the probability of collision, so this scenario selects a random uniform sample of 1000 relative velocity magnitudes on the interval $[5, 15][km/s]$. The relative velocity direction is computed by a uniform random sample of 1000 unit vector directions. This stochastic approach to modeling potential conjunction geometries is critical for getting a fuller picture of potential maneuver decisions. To keep the example simple, the state covariance matrix for the secondary object at TCA in all cases is the same as the covariance of the primary, just oriented in the RIC frame with respect to the secondary object rather than the primary. Still, the assumption that the covariances are not correlated when computing the probability of collision is retained for a more realistic Pc evaluation.

Figure 9 shows the probability that the computed Pc exceeds a maneuver threshold of 1×10^{-5} as a function of time until TCA for each of the four cases. If a maneuver decision needed to be made n days prior to TCA, the figure shows what decision might be made for each of the four cases. Figure 9a shows maneuver decision probabilities by case at an altitude of 450 km, while 9b and 9c show 550 and 650 km, respectively. First, it is clear that it is difficult to make correct maneuver decisions early at 450 km under any circumstance, even if forecast models are improved significantly. The baseline from case (1) shows that a correct maneuver decision cannot be reliably made until only three hours prior to TCA. Even removing uncertainty in $F10.7$ altogether in case (2) provides only a few hours of additional notice. Reducing the uncertainty in ap in case (3) makes further modest improvements on maneuver notice while introducing a bias on ap does not seem to have much impact on the overall decision notice.

At the 550 km altitude, it is clear that there is significantly more advance notice for maneuvering when provided with better forecasts. For the baseline case (1), reliable maneuver notice is up from 3 hours to about 12 hours. The benefit of forecasting $F10.7$ perfectly is clearly apparent in this plot by comparing case (2) to case (1). Case (2) maneuver notice leads case (1) by about a day, meaning that an operator could decide to maneuver for this event much sooner with the same risk posture if they had this perfect forecast for $F10.7$ available. Further reducing the uncertainty in the ap forecasts leads to even more advance maneuver notice, but adding a small bias now has a significant negative impact.

At the 650 km altitude, these effects are even more apparent. In all cases, the maneuver decision can be reliably made about 1 day prior to TCA. There is about a two-day difference in maneuver notice between cases (1) and (2), and the bias on ap in case (4) significantly reduces decision-making performance to something comparable to case (1). At this higher altitude, the overall neutral density is much less than that at 450 km,

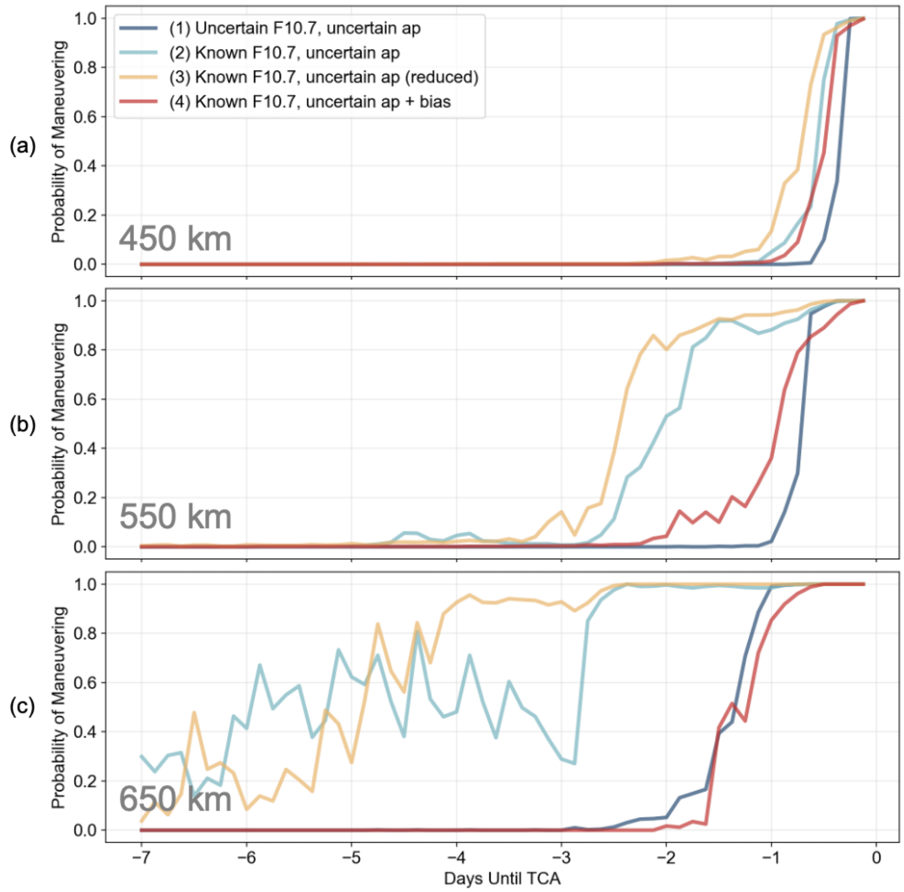

Figure 9. Probability of maneuvering for a conjunction event that ends in a collision as a function of time from TCA. Maneuver decisions are based on a Pc threshold of 1×10^{-5} and each case is demonstrated at (a) 450 km, (b) 550 km, and (c) 650 km to show altitude dependence.

and variability in density is more strongly forced by EUV absorption and enhanced geomagnetic activity. At higher altitudes, it matters less and less what forecast model is being used as the time to TCA wanes, especially when the maneuver decision is being made less than one day prior to TCA, since it takes a long time for satellite position errors to accumulate.

7 Conclusion

As long as the standard practice in operations is to continue to delay maneuver decision-making until 12-24 hours prior to TCA, this effort shows that there is little value that comes from improving space weather forecasts, especially at higher altitudes above 500 km during average solar conditions (mid-cycle). During solar maximum, the lower boundary for altitude where improved forecasts make a significant difference is even higher. It takes time for forecasted density errors to translate to accumulated satellite state errors, and this is especially true at higher altitudes. Although relative variability in the neutral density is greater at higher altitudes, drag is also less impactful in deviating satellite state. Considering, however, that there is appetite within the spacecraft operator community for maneuvering sooner, this effort shows that better space weather forecasts have the potential to provide significant improvements in advance notice in the case of dangerous conjunction events, especially at the middle LEO altitudes where most large constellations plan to operate. The utility of these forecast improvements will also vary depending on operating altitude and the state of the solar cycle.

There is great potential for improving the fusion of space weather forecast information into the conjunction assessment pipeline. In particular, the authors recommend that space weather organizations provide not only forecasted indices and densities but also uncertainties associated with these forecasts rooted in measurement uncertainties or physical quantities rather than empirical error performance. As is, some operators are subject to considering forecasts as truth, which dangerously leads to poor covariance realism in the conjunction assessment process. Accurately reflecting the uncertainty in the indices and forecasted densities may be challenging, considering that the uncertainties are often non-Gaussian and heteroscedastic. Accurately modeling these uncertainties and the impact they have on Pc, especially if the Gaussian state uncertainty assumption is violated, are important areas of continuing work.

Open Research Section

Historical TLEs for tracked objects are publicly available through space-track.org. Partial historical CDMs were accessed and are available from https://kelvins.esa.int/collision-avoidance-challenge/data/. A history of the recorded solar and geomagnetic indices is available at https://kp.gfz-potsdam.de/en/data.

Acknowledgments

This work was supported by the National Science Foundation Graduate Research Fellowship under Grant No. 1745302 and the National Science Foundation under award NSF-PHY-2028125. The authors gratefully acknowledge the sponsors for their support.

References

Alfano, S. (2005). A numerical implementation of spherical object collision probability. *The Journal of the Astronautical Sciences*, *53*, 103–109.

Alfano, S. (2007). Review of conjunction probability methods for short-term encounters (aas 07-148). *Advances in the Astronautical Sciences*, *127*(1), 719.

Aristoff, J. M., Cox, C. M., NASA, J. H. F., Grumman, R. W. G. N., Horwood, J. T., Jah, M. K., … AGI, J. W. W. (2016). *Covariance and uncertainty realism in space surveillance and tracking.*

Barker, W. N., Casali, S. J., & Walker, C. A. (2000). Improved space surveillance network observation error modeling and techniques for force model error mitigation. *Astrodynamics 1999*, 1881–1901.

Bartels, J. (1949). The standardized index, ks, and the planetary index, kp. *IATME bull*, *97*(0001).

Bowman, B. (2002). True satellite ballistic coefficient determination for hasdm. In *Aiaa/aas astrodynamics specialist conference and exhibit* (p. 4887).

Bussy-Virat, C. D., Ridley, A. J., & Getchius, J. W. (2018, 5). Effects of uncertainties in the atmospheric density on the probability of collision between space objects. *Space Weather*, *16*, 519-537. doi: 10.1029/2017SW001705

Chan, K. (1997). Collision probability analysis for earth orbiting satellites. *Space cooperation into the 21 st century*, 1033–1048.

Consultative Committee for Space Data Systems. (2022). *Conjunction data message (cdm) pink book.* Retrieved from `https://cwe.ccsds.org/moims/docs/MOIMS-NAV/Draft%20Documents/Conjunction%20Data%20Message%20(CDM)/508x0p1.0.3_CDM_Changes_Accepted.pdf` (508x0p1.0.3_CDM_Changes_Accepted.pdf)

Covington, A. (1948). Solar noise observations on 10.7 centimeters. *Proceedings of* *the IRE*, *36*(4), 454-457. doi: 10.1109/JRPROC.1948.234598

Davis, E., Dunn, C., Stanton, R., & Thomas, J. (2000). *The grace mission: meeting the technical challenges* (Tech. Rep.).

Dickey, M. R., & Culp, R. D. (1989). Determining characteristic mass for low-earth-orbiting debris objects. *Journal of Spacecraft and Rockets*, *26*(6), 460–464.

Doornbos, E., Förster, M., Fritsche, B., van Helleputte, T., van den IJssel, J., Koppenwallner, G., ... Kern, M. (2009). Air density models derived from multi-satellite drag observations. In *Proceedings of esas second swarm international science meeting. potsdam* (Vol. 24).

Emmert, J., Dhadly, M., & Segerman, A. (2021). A globally averaged thermospheric density data set derived from two-line orbital element sets and special perturbations state vectors. *Journal of Geophysical Research: Space Physics*, *126*(8), e2021JA029455.

Emmert, J. T., Warren, H., Segerman, A., Byers, J., & Picone, J. (2017). Propagation of atmospheric density errors to satellite orbits. *Advances in Space Research*, *59*(1), 147–165.

Foster, J. L., & Estes, H. S. (1992). *A parametric analysis of orbital debris collision probability and maneuver rate for space vehicles.* NASA, National Aeronautics and Space Administration, Lyndon B. Johnson Space Cene.

Gondelach, D. J., Armellin, R., & Lidtke, A. A. (2017). Ballistic coefficient estimation for reentry prediction of rocket bodies in eccentric orbits based on tle data. *Mathematical Problems in Engineering*, *2017*.

Gondelach, D. J., Linares, R., & Siew, P. M. (2022). Atmospheric density uncertainty quantification for satellite conjunction assessment. *Journal of Guidance, Control, and Dynamics*, *45*(9), 1760–1768.

Hejduk, M. (2019). Three ca-related covariance issues and their solutions. In *Cnes international conjunction assessment workshop.*

Hejduk, M. D., & Snow, D. E. (2018, 7). The effect of neutral density estimation errors on satellite conjunction serious event rates. *Space Weather*, *16*, 849-869. doi: 10.1029/2017SW001720

Hejduk, M. D., & Snow, D. E. (2019). *Satellite conjunction assessment risk analysis for "dilution region" events: Issues and operational approaches.*

Henney, C., Hock, R., Schooley, A., Toussaint, W., White, S., & Arge, C. (2015). Forecasting solar extreme and far ultraviolet irradiance. *Space Weather*, *13*(3), 141–153.

Henney, C., Toussaint, W., White, S., & Arge, C. (2012). Forecasting f10. 7 with solar magnetic flux transport modeling. *Space Weather*, *10*(2).

Hoots, F. R. (1980). Spacetrack report no. 3, models for propagation of norad element sets. *http://www. itc. nl/-bakker/orbit. html*.

Lean, J., Picone, J., & Emmert, J. (2009). Quantitative forecasting of near-term solar activity and upper atmospheric density. *Journal of Geophysical Research: Space Physics*, *114*(A7).

Licata, R. J., Tobiska, W. K., & Mehta, P. M. (2020). Benchmarking forecasting models for space weather drivers. *Space Weather*, *18*(10), e2020SW002496.

Linares, R., Crassidis, J. L., & Jah, M. K. (2014). Particle filtering light curve based attitude estimation for non-resolved space objects. In *Aas/aiaa space flight mechanics meeting* (pp. 14–210).

Moomey, L. C. D., Falcon, R., & Khan, A. (2023). Trending and analysis of payload vs. all low earth conjunction data messages below 1000 km, from 2016 through 2021. *Journal of Space Safety Engineering*, *10*(2), 217–230.

NASA. (2023, March). *Cost and Benefit Analysis of Orbital Debris Remediation.* `https://www.nasa.gov/sites/default/files/atoms/files/otps_-_cost_and_benefit_analysis_of_orbital_debris_remediation_-_final.pdf`. (Accessed: April 7, 2023)

Patera, R. P. (2001). General method for calculating satellite collision probability. *Journal of Guidance, Control, and Dynamics*, *24*(4), 716–722.

Picone, J., Hedin, A., Drob, D. P., & Aikin, A. (2002). Nrlmsise-00 empirical model of the atmosphere: Statistical comparisons and scientific issues. *Journal of Geophysical Research: Space Physics*, *107*(A12), SIA–15.

Poore, A. B., Aristoff, J. M., Horwood, J. T., Armellin, R., Cerven, W. T., Cheng, Y., … others (2016). Covariance and uncertainty realism in space surveillance and tracking. *Report of the Air Force Space Command Astrodynamics Innovation Committee*, *27*.

Reigber, C., Schwintzer, P., Lühr, H., et al. (1999). The champ geopotential mission. *Boll. Geof. Teor. Appl*, *40*, 285–289.

Saunders, A., Swinerd, G. G., & Lewis, H. G. (2012). Deriving accurate satellite ballistic coefficients from two-line element data. *Journal of Spacecraft and Rockets*, *49*(1), 175–184.

Schildknecht, T., Silha, J., Pittet, J.-N., & Rachman, A. (2017). Attitude states of space debris determined from optical light curve observations.

Shprits, Y. Y., Vasile, R., & Zhelavskaya, I. S. (2019, August). Nowcasting and Predicting the Kp Index Using Historical Values and Real-Time Observations. *Space Weather*, *17*(8), 1219-1229. doi: 10.1029/2018SW002141

Šilha, J. (2020). Space debris: optical measurements. *Reviews in Frontiers of Modern Astrophysics: From Space Debris to Cosmology*, 1–21.

Šilha, J., Pittet, J.-N., Hamara, M., & Schildknecht, T. (2018). Apparent rotation properties of space debris extracted from photometric measurements. *Advances in space research*, *61*(3), 844–861.

Stevenson, E., Rodriguez-Fernandez, V., Minisci, E., & Camacho, D. (2022). A deep learning approach to solar radio flux forecasting. *Acta Astronautica*, *193*, 595–606.

Tapping, K. (2013). The 10.7 cm solar radio flux (f10. 7). *Space weather*, *11*(7), 394–406.

Uriot, T., Izzo, D., Simões, L. F., Abay, R., Einecke, N., Rebhan, S., … Merz, K. (2022). Spacecraft collision avoidance challenge: Design and results of a machine learning competition. *Astrodynamics*, *6*(2), 121–140.

Vallado, D. A. (2001). *Fundamentals of astrodynamics and applications* (Vol. 12). Springer Science & Business Media.

Wang, W., Burns, A., Wiltberger, M., Solomon, S., & Killeen, T. (2008). Altitude variations of the horizontal thermospheric winds during geomagnetic storms. *Journal of Geophysical Research: Space Physics*, *113*(A2).

Zhang, S. P., & Shepherd, G. G. (2000). Neutral winds in the lower thermosphere observed by windii during the april 4–5th, 1993 storm. *Geophysical research letters*, *27*(13), 1855–1858.

Figure 1.

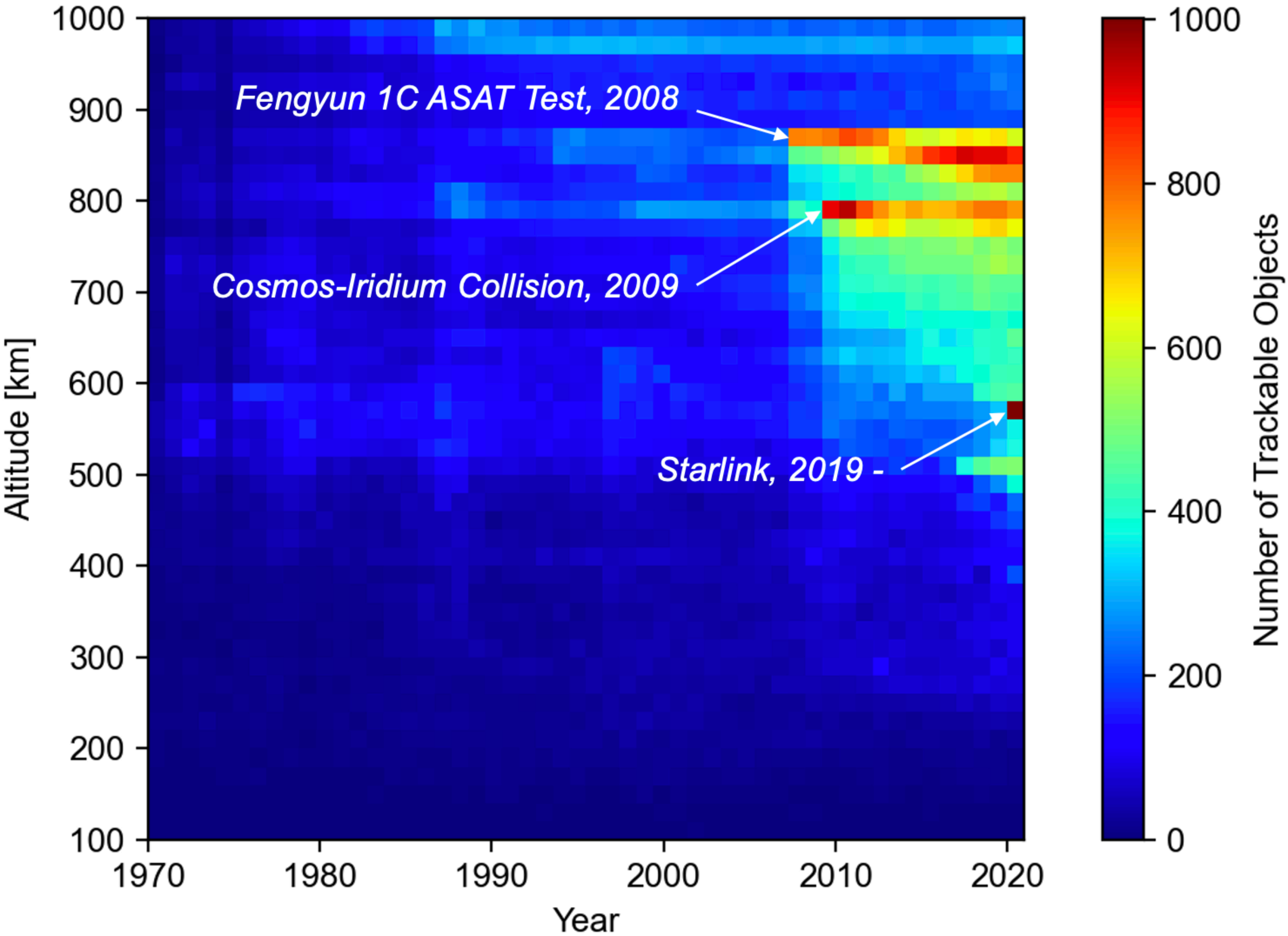
Fengyun 1C ASAT Test, 2008
Cosmos-Iridium Collision, 2009
Starlink, 2019 -
Altitude [km]
Year
Number of Trackable Objects
1000
900
800
700
600
500
400
300
200
100
1970
1980
1990
2000
2010
2020
1000
800
600
400
200
0

Figure 2.

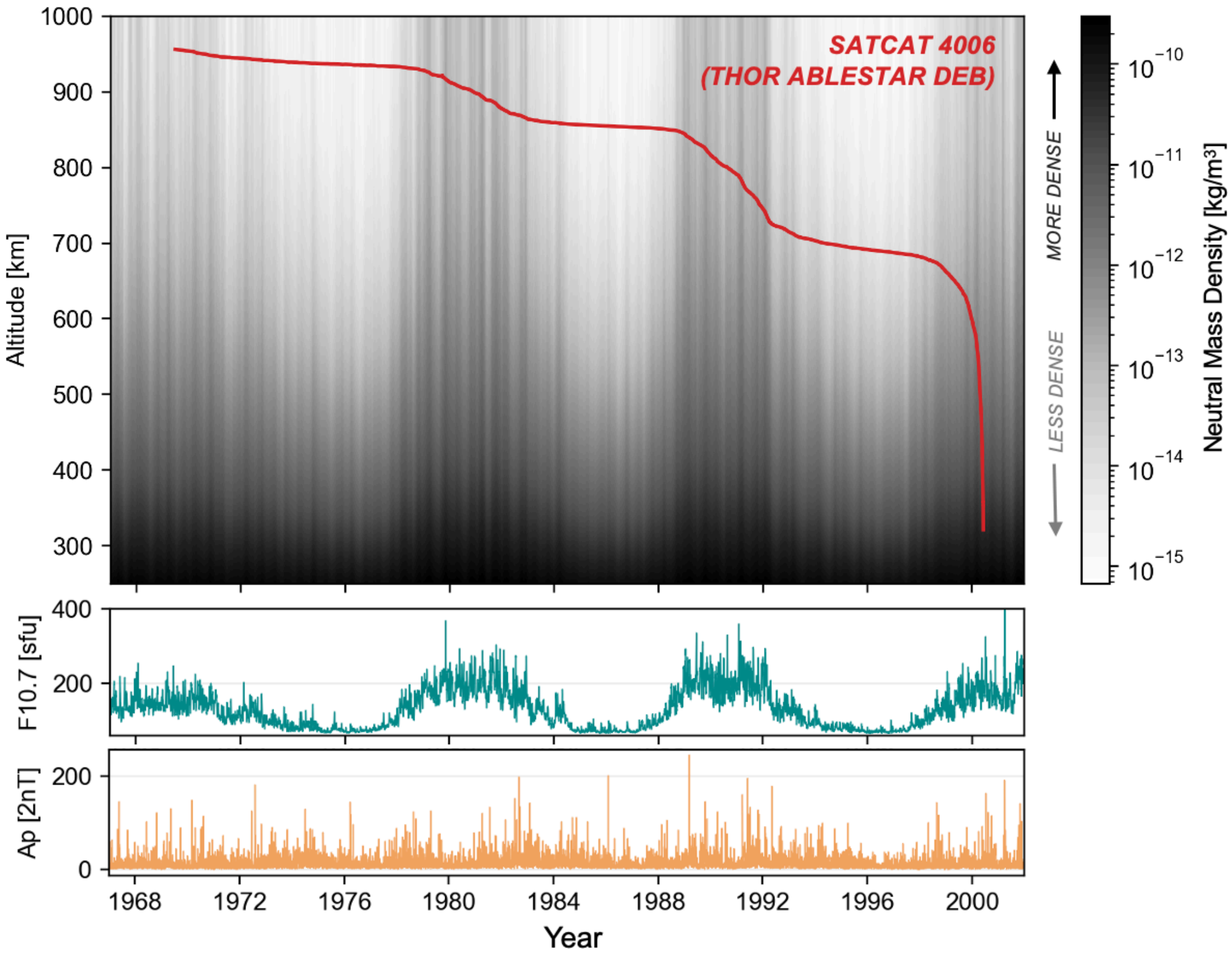

SATCAT 4006
(THOR ABLESTAR DEB)
Altitude [km]
1000
900
800
700
600
500
400
300
MORE DENSE
LESS DENSE
Neutral Mass Density [kg/m³]
10^−10
10^−11
10^−12
10^−13
10^−14
10^−15
F10.7 [sfu]
400
200
Ap [2nT]
200
0
1968
1972
1976
1980
1984
1988
1992
1996
2000
Year

Figure 3.

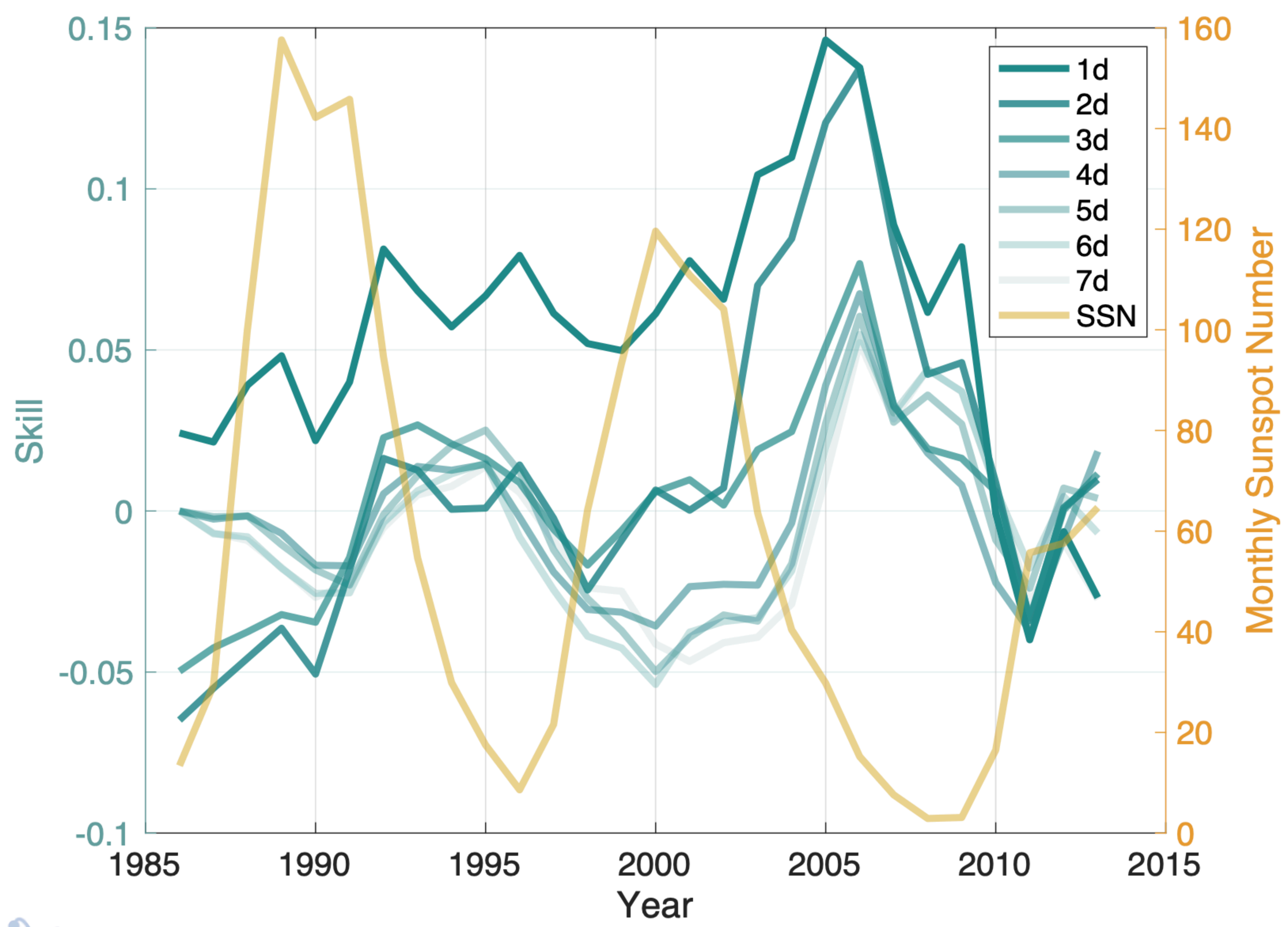

Skill
0.15
0.1
0.05
0
-0.05
-0.1
1985
1990
1995
2000
2005
2010
2015
Year
Monthly Sunspot Number
160
140
120
100
80
60
40
20
0
1d
2d
3d
4d
5d
6d
7d
SSN

Figure 4.

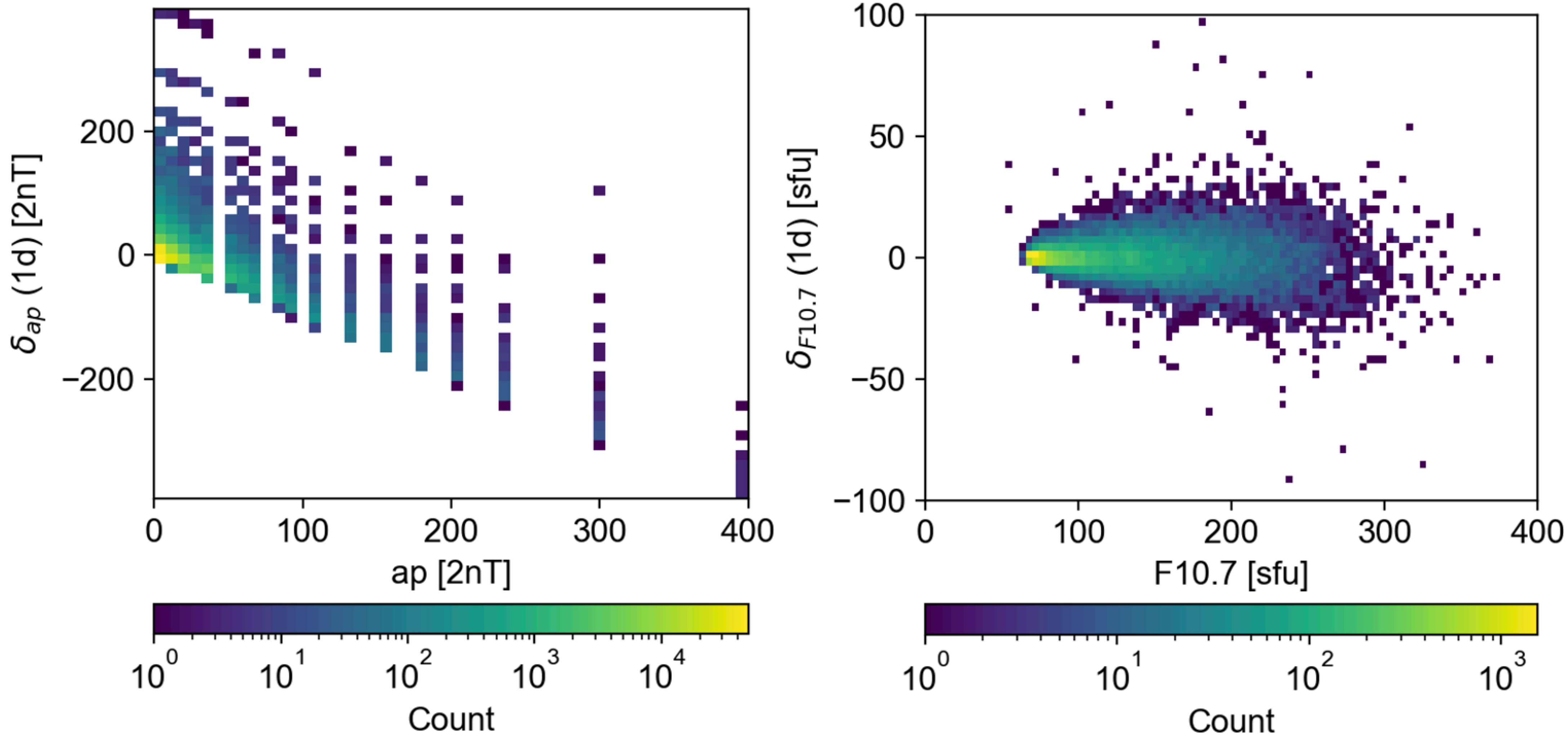

(a) (b)

Figure 5.

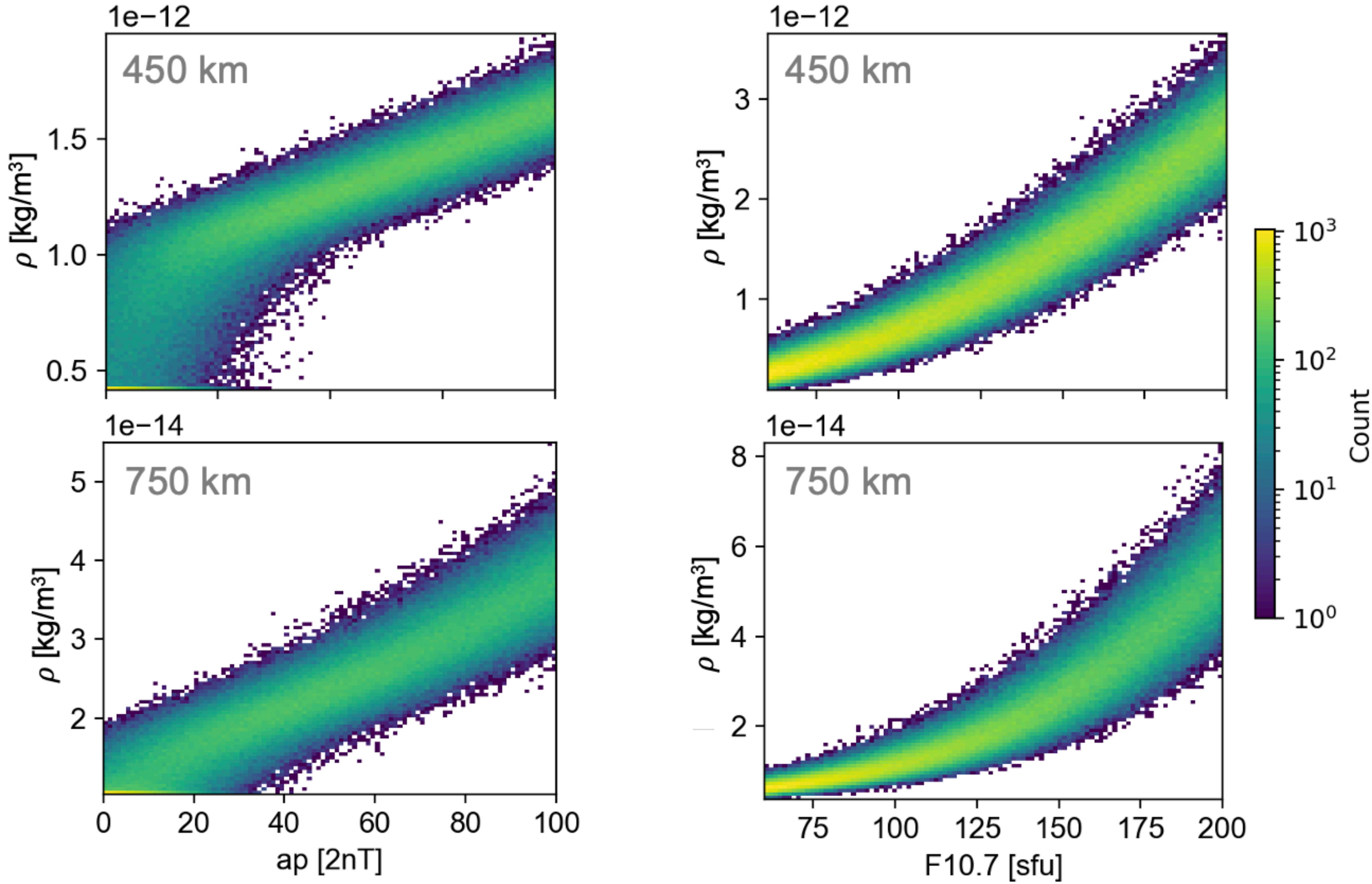

(a)
F10.7 = 120 [sfu]
F10.7A = 120 [sfu]
ap = $\mathcal{N}$(x, 10^2) [2nT]

(b)
F10.7 = $\mathcal{N}$(x, 10^2) [sfu]
F10.7A = x [sfu]
ap = 20 [2nT]

Figure 6.

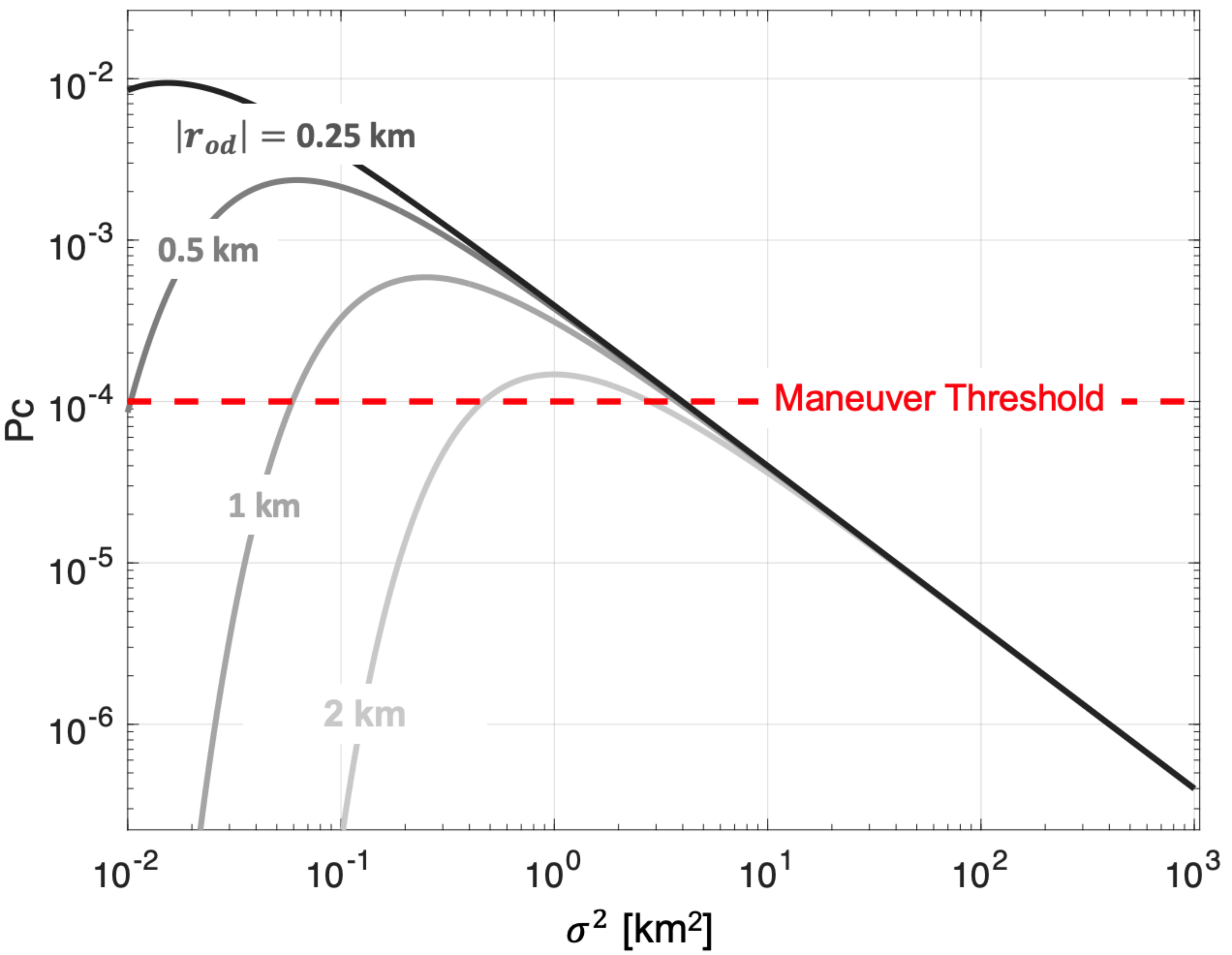

$|r_{od}| = 0.25$ km
0.5 km
1 km
2 km
Maneuver Threshold
Pc
10^{-2}
10^{-3}
10^{-4}
10^{-5}
10^{-6}
10^{-2}
10^{-1}
10^{0}
10^{1}
10^{2}
10^{3}
σ^2 [km^2]

Figure 7.

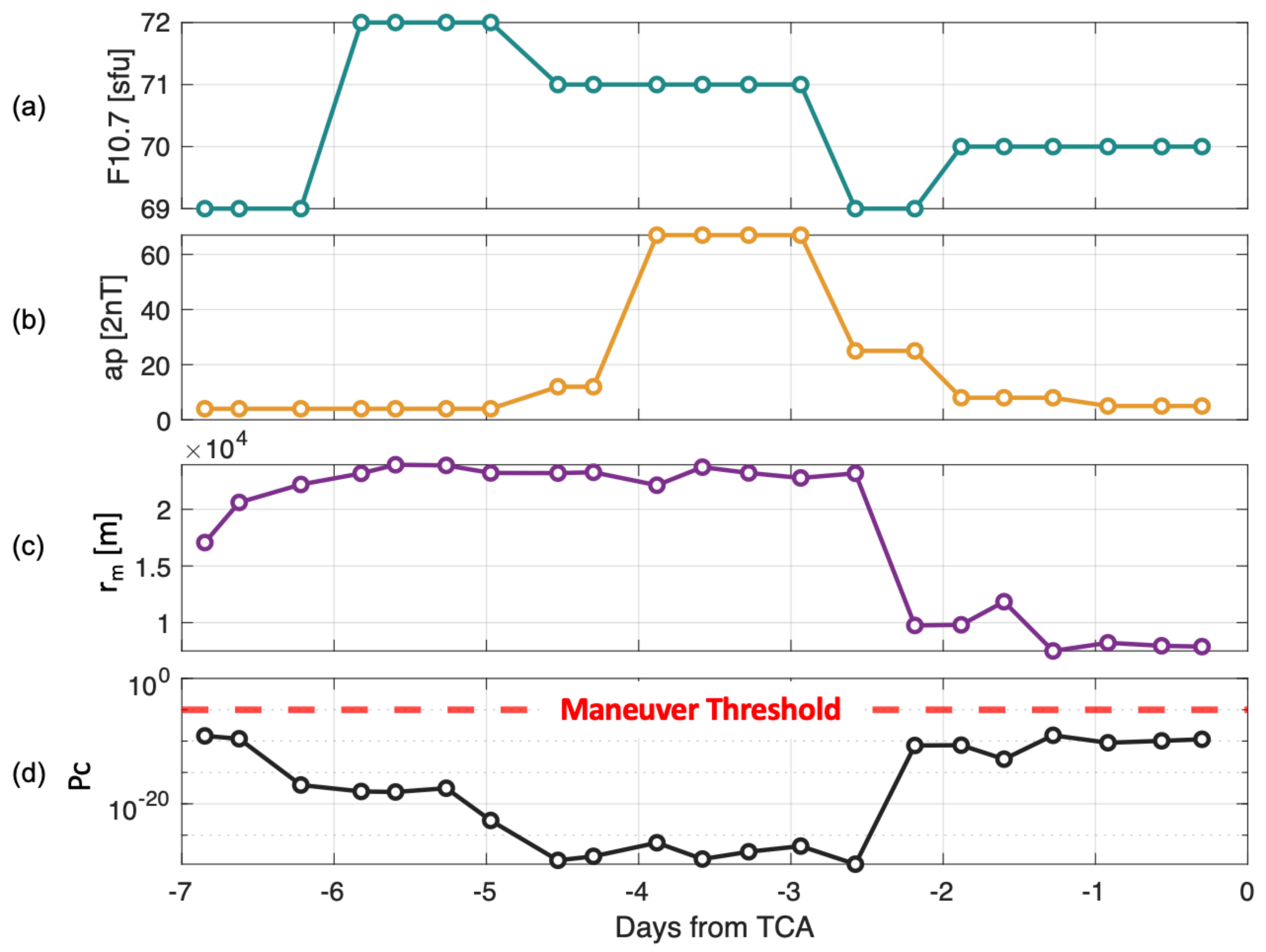

(a)
F10.7 [sfu]
72
71
70
69
(b)
ap [2nT]
60
40
20
0
(c)
×10^4
r_m [m]
2
1.5
1
(d)
Pc
10^0
10^-20
Maneuver Threshold
-7
-6
-5
-4
-3
-2
-1
0
Days from TCA

Figure 8.

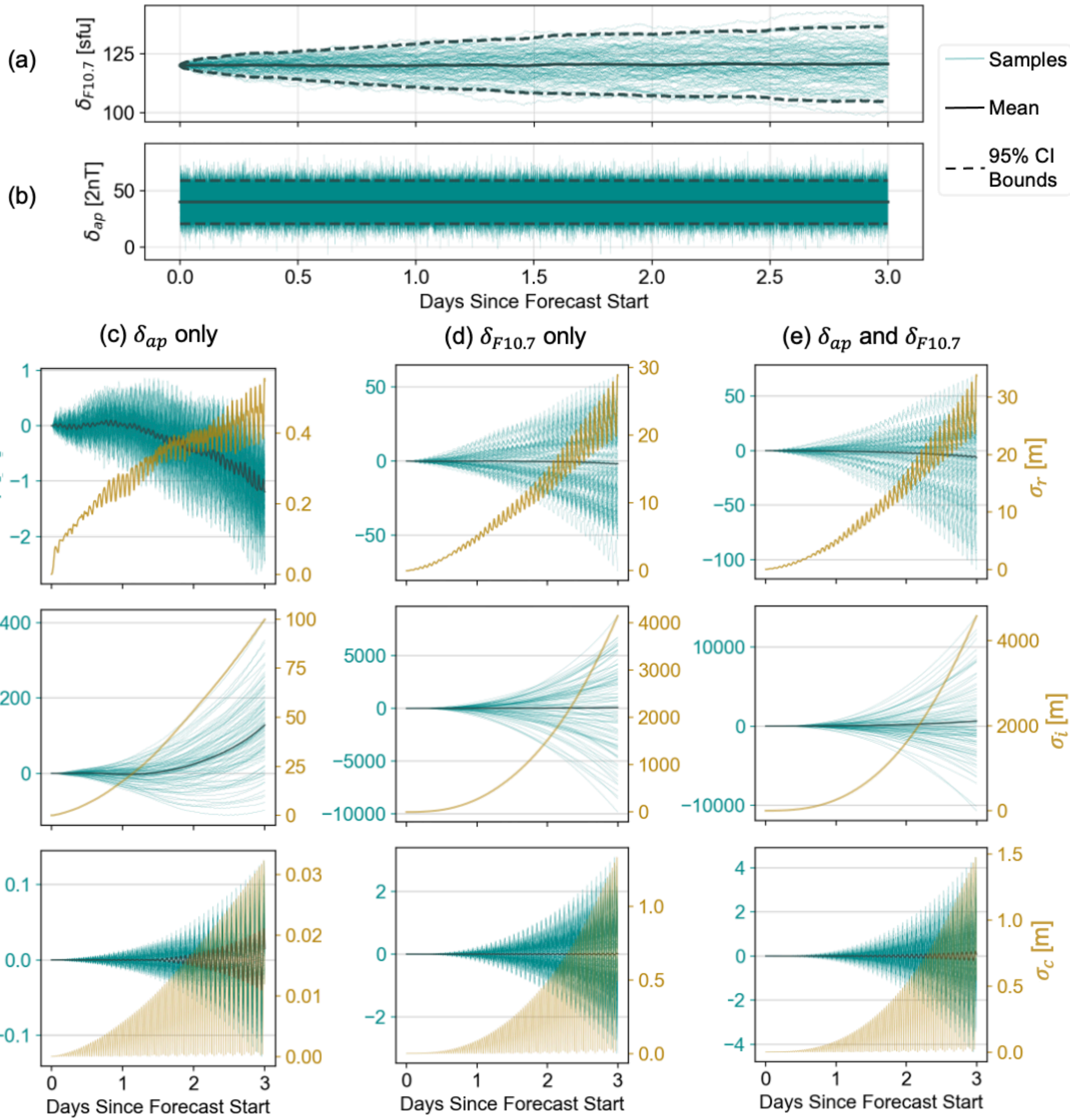

(a)
$\delta_{F10.7}$ [sfu]
(b)
δ_{ap} [2nT]
Days Since Forecast Start
Samples
Mean
95% CI Bounds
(c) δ_{ap} only
(d) $\delta_{F10.7}$ only
(e) δ_{ap} and $\delta_{F10.7}$
δ_r [m]
σ_r [m]
δ_i [m]
σ_i [m]
δ_c [m]
σ_c [m]
Days Since Forecast Start
Days Since Forecast Start
Days Since Forecast Start

Figure 9.

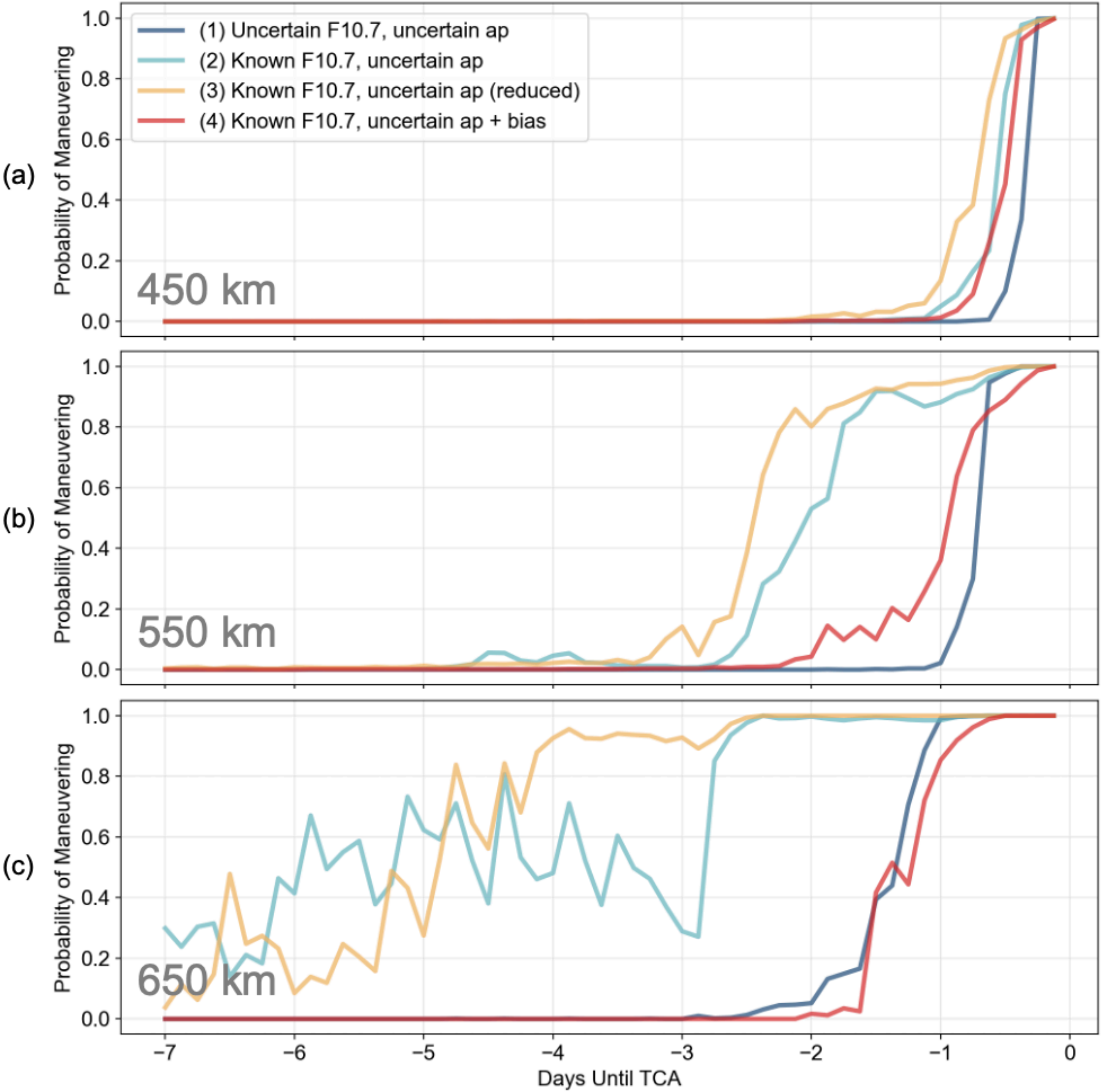

(1) Uncertain F10.7, uncertain ap
(2) Known F10.7, uncertain ap
(3) Known F10.7, uncertain ap (reduced)
(4) Known F10.7, uncertain ap + bias
(a)
(b)
(c)
450 km
550 km
650 km
Probability of Maneuvering
Days Until TCA